A novel method for the accurate characterization of transport and structural parameters of deformable membranes utilized in pressure- and osmotically driven membrane processes

Christian D. Peters[a,b], Daniel Yee Fan Ng[b], Nicholas P. Hankins[a,*], Qianhong She[b,c,*]

[a]*Department of Engineering Science, The University of Oxford, Parks Road, OX3 1PJ, Oxford, UK*
[b]*Singapore Membrane Technology Centre, Nanyang Environment & Water Research Institute, Nanyang Technological University, Singapore*
[c]*School of Civil and Environmental Engineering, Nanyang Technological University, 50 Nanyang Avenue, 639798, Singapore*

Abstract

Membrane deformation is a common phenomenon in pressurized membrane processes. It alters the transport and structural characteristics of membranes and hence can lead to a lower than estimated process performance. Therefore, it is essential to accurately characterize the membrane under representative operating conditions. This will allow for both an understanding of the underlying mechanisms for the change of membrane performance, and an optimization of the design and operation of pressure- and osmotically driven membrane processes. A novel membrane characterization method is proposed, validated and tested in this study. Using the osmotic-resistance filtration model, the membrane's water and solute permeability (A and B), as well as its structural parameter S, can be accurately determined using the method. The method is named the integrated two-stage (ITS) ABS method, as the membrane can be fully characterized at any given pressure using a single continuous test that is divided into two stages; each stage uses a different feed or draw concentration. A, B and S are calculated from the experimentally determined water and solute fluxes by performing a least-squares non-linear regression. The proposed method is robust, simple and offers more accurate predictions of the membrane's transport and structural properties than the currently most widely used reverse osmosis-forward osmosis (RO-FO) characterization method.

Keywords: Membrane properties; Membrane deformation; Reverse osmosis; Osmotically assisted reverse osmosis; Pressure retarded osmosis; Pressure assisted osmosis

1. Introduction

Membrane processes that operate at high transmembrane pressures and/or utilize membranes with a thin and porous substrate, such as osmotically assisted reverse osmosis (OARO) [1, 2, 3], pressure retarded osmosis (PRO) [4, 5, 6, 7], high-pressure reverse osmosis (HPRO) [8, 9], and pressure assisted osmosis (PAO) [10, 11, 12, 13], are plagued by membrane deformation. It has been recognized that severe membrane deformation could drastically deteriorate membrane performance by altering the membrane intrinsic properties; namely its water permeability A, solute permeability B, water/solute selectivity B/A and its structural parameter S.

Recently, Davenport et al. [8] recorded a 35% reduction in the water permeability of commercially available reverse osmosis (RO) membranes, as the operating pressure was increased from 70 bar to 150 bar. The main cause for this decline in water permeability was identified as membrane compaction, which led to a 95% reduction in the surface porosity of the membrane's support layer. Similar findings were reported by Aghajani et al. [14], who found that the support layer porosity decreased as it yielded at high operating pressures, and this increased the overall permeation resistance of the utilized TFC membranes. Furthermore, de Roever et al. [15] found that compaction and spacer intrusions in the membrane are a common phenomenon in spiral-wound RO membrane modules after year-long operation. In particular, they found that deeper spacer intrusions are more likely to be found in membrane modules operated at high temperatures and pressures.

While membrane compression and the associated loss in permeability is common in a well supported membrane with a thicker and less porous substrate and a less open spacer backing, an increase in the water and solute permeability is also possible for a membrane with a thinner and more porous substrate and a more open spacer backing. The latter outcome was demonstrated by Idarraga-Mora et al. [16], Madsen et al. [4], She et al. [17] and She et al. [18]. A thinner membrane with an open spacer backing is prone to membrane deformation by coupled tensile stretching and hydraulic compression [17], which can lead to 1) the displacement and elongation of polymer chains in the membrane's active and support layers, 2) an increase in active membrane area and even 3) to the breakage of chain covalent bonds within the polymer crystallites. All of these effects can lead to changes in the membrane's intrinsic properties [19, 20].

As highlighted by the above studies, membrane deformation can considerably affect the performance of HPRO, OARO, PRO and PAO processes. Hence, it is critically important to accurately characterize the membrane properties under repre-

*Corresponding authors
Email addresses: nick.hankins@eng.ox.ac.uk (Nicholas P. Hankins), qhshe@ntu.edu.sg (Qianhong She)

sentative operating conditions in order to improve upon the current designs of these processes. Currently, there are in the main three different membrane characterization techniques available: 1) the conventional RO and RO-FO method [21, 22], 2) the characterization method developed by Tiraferri et al. [23] specifically for forward osmosis, and 3) its adaptation for PRO processes, which was investigated by Kim et al. [24].

The conventional RO method is widely used by membrane manufacturers to report the parameters related to the membrane's active layer (A and B). While this method was initially developed to characterize membranes intended for purely pressure-driven operation, it has since been widely adopted in the literature to determine A and B for membranes intended for osmotic operation [21]. In this case, however, another forward osmosis (FO) experiment is required to determine the membrane's structural parameter. However, as stated by Tiraferri et al. [23], this conventional RO-FO approach is inadequate to accurately determine the intrinsic properties of FO membranes, as the membranes are subjected to high pressures in the RO tests which far exceed the transmembrane pressures in normal FO operation. Many other studies also show that experimental and modelled water and solute fluxes do not correlate well when using membrane parameters determined by the conventional RO-FO method [25, 13, 26, 18]. In addition, the conventional characterization approaches are laborious, and require multiple experiments, different experimental setups and varying operating conditions that may significantly differ from the actual operating conditions of the membrane process.

On the other hand, membrane properties are determined using a single FO experiment by Tiraferri et al. [23], in which the water and solute fluxes are recorded at ambient pressure and for four different draw solution concentrations. A, B and S are then determined from those measurements by performing a least-squares non-linear regression. Similarly, Kim et al. [24] adopted this approach for PRO and determined A, B and S for a PRO membrane at different operating pressures. This method is less cumbersome and more accurate than the conventional RO-FO approach, but still requires four different draw solute concentrations to be tested.

In the present study, a novel membrane characterization technique is presented that further simplifies the experimental procedure presented earlier by Tiraferri et al. [23] to accurately determine A, B and S either at any given operational pressure or as a function of the transmembrane pressure. This method is especially beneficial for the characterization of those membranes, or even entire membrane modules, that may undergo severe deformation and hence experience changes of A, B and S with the transmembrane pressure.

In brief, the characterization approach presented here requires only two concentration stages instead of four to accurately characterize membranes utilized in pressurized membrane systems. As either the feed or draw are pressurized, deionised water can be used to directly calculate A at the given operational pressure. B and S are then subsequently determined by increasing the feed concentration, with the operational pressure unchanged, and using the recorded water and solute fluxes to solve the rearranged membrane transport equations.

2. Description of the proposed membrane characterization method

2.1. Membrane transport equations

Figure 1 shows the concentration profiles with internal concentration polarisation (ICP) and external concentration polarisation (ECP) in asymmetric membranes. The typical membrane orientations for each membrane process are shown. These are widely used to prevent the intrusion of the spacer backing into the membrane's active layer under high applied pressures, which can lead to membrane damage [12, 7]. Therefore, the active layer preferentially faces the pressurized solution, i.e. active layer facing feed side (AL-FS) for RO, HPRO, PAO and OARO, and active layer facing draw side (AL-DS) for PRO. It should be noted that the opposite membrane orientation, where the support layer faces the pressurized solution, is also applicable under certain operating conditions. Particularly for PRO, the AL-FS membrane orientation has been widely investigated for fouling control under high fouling conditions [27, 28, 29, 30].

In this study, the osmotic resistance filtration (ORF) model (equation (1) to equation (3)) is used to universally describe all of the aforementioned osmosis-related processes, regardless of the chosen membrane orientation. Based on the universal ORF model, the membrane intrinsic transport and structural parameters can be characterized using the integrated two-stage (ITS) ABS method developed in this study.

According to She et al. [31], the ORF model subdivides the driving forces across the membrane into different components, i.e., apparent driving force F_{App}, driving force loss due to concentrative concentration polarisation (CCP) F_{CCP}, and driving force loss due to dilutive concentration polarisation (DCP) F_{DCP}. The effective driving force is then taken as the difference between the apparent driving force and the sum of the driving force losses:

$$J_W = A\left(F_{App} - F_{CCP} - F_{DCP}\right) \tag{1}$$

For the indicated directions of the water flux J_W, solute flux J_S and the transmembrane hydraulic pressure ΔP and osmotic pressure $\Delta\pi$ of the HPRO and OARO processes in figure 1, equation (1) can be mathematically expressed as:

$$\begin{aligned} J_W \;=\; & A\Big((\Delta P - \Delta\pi) \\ & - f_{CCP}\left(\pi_F - \tfrac{J_S}{J_W}\beta R_G T\right) \\ & - f_{DCP}\left(\pi_D - \tfrac{J_S}{J_W}\beta R_G T\right)\Big) \end{aligned} \tag{2}$$

Equation (2) indicates that the concentration polarisation terms are not only affected by the convective conditions in the feed and draw solutions but also by the solute diffusion across the membrane (i.e., in terms of J_S/J_W) [32]. In PAO and PRO, the reverse solute diffusion (from the draw to the feed solution) exacerbates both CCP and DCP, and thus leads to the decrease of the water flux. On the other hand, forward solute diffusion (from the feed to the draw) solution reduces both CCP and DCP and hence compensates driving force losses in HPRO

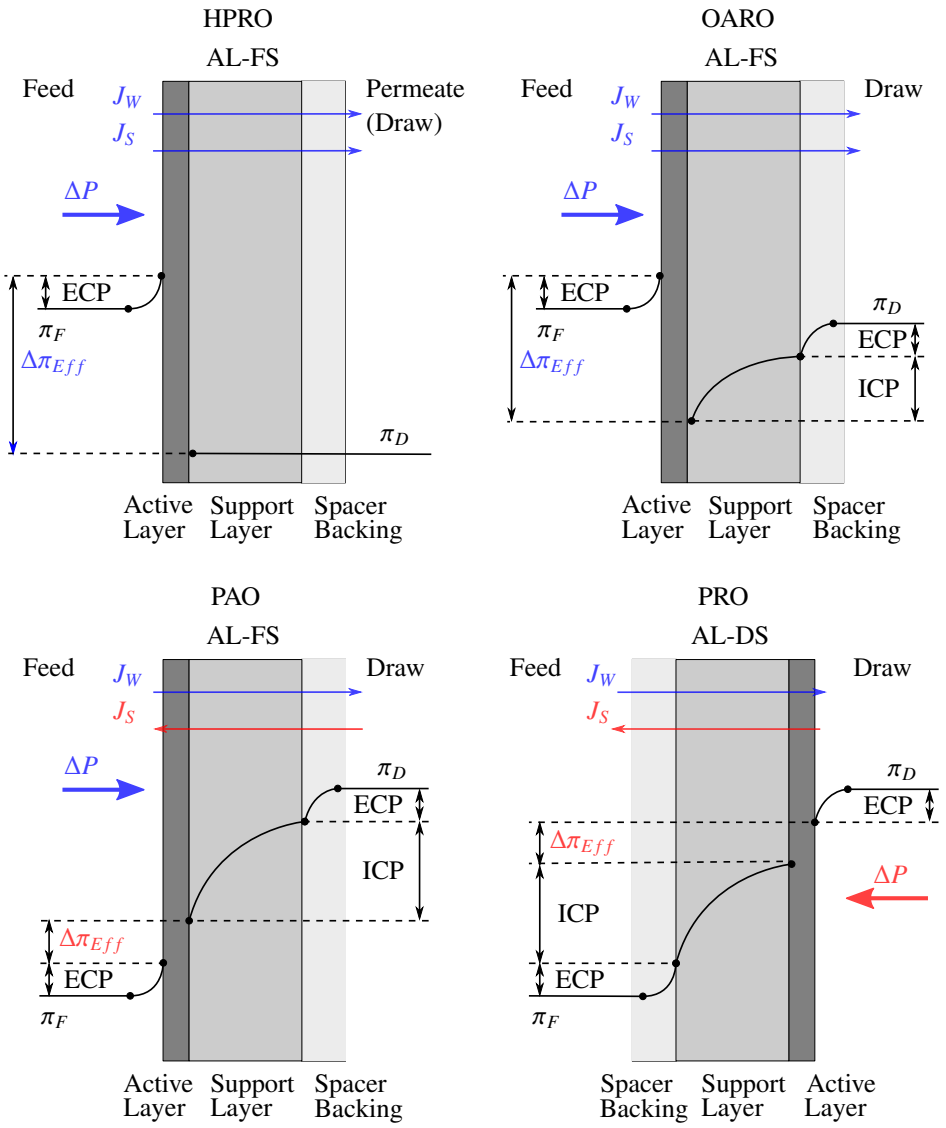

Figure 1: Concentration profile for typical membrane orientations for HPRO, OARO, PAO and PRO membrane processes. In HPRO and OARO the effective osmotic pressure $\Delta\pi_{Eff}$ is positive (indicated in blue), as the permeate (draw) is less concentrated than the feed. On the other hand, $\Delta\pi_{Eff}$ is negative (indicated in red) for PAO and PRO, as the draw is more concentrated than the feed. Note that in OARO, the osmotic back pressure has been reduced by the draw solution compared to HPRO, while in PRO the hydraulic pressure has been reversed compared to PAO.

and OARO operation. However, an increase in forward solute diffusion reduces the useful work done by the system, resulting in a reduced 2nd law efficiency [2], and is indicative of a lower membrane selectivity. Specifically, J_S/J_W in equation (2) can be described by the following equation [31]:

$$\frac{J_S}{J_W} = \frac{B}{A\beta R_G T}\left(\frac{A\Delta P}{J_W} - 1\right) \tag{3}$$

Equation (2) and equation (3) have both been derived on the assumption that the bulk osmotic pressure of the feed (π_F) and draw (π_D) solution can be related to their concentrations (C_F and C_D) using:

$$\pi = \beta R_G T C \tag{4}$$

where β, R_G T and C are the van't Hoff factor, the universal gas constant, the fluid temperature and the solution concentration, respectively. The CCP factor f_{CCP} and the DCP factor f_{DCP} can be expressed by the following equations:

$$f_{CCP} = exp\left(\frac{J_W}{k_{CCP}}\right) - 1 \tag{5}$$

and

$$f_{DCP} = 1 - exp\left(\frac{-J_W}{k_{DCP}}\right) \tag{6}$$

where $1/k_{CCP}$ and $1/k_{DCP}$ represent the induced mass transfer resistances due to concentrative and dilutive concentration polarisation, respectively. For the AL-FS membrane orientation, $1/k_{CCP}$ and $1/k_{DCP}$ are given by:

$$1/k_{CCP} = 1/k_F \tag{7}$$

and

$$1/k_{DCP} = (1/k_M + 1/k_D) \tag{8}$$

where k_F and k_D are the mass transfer coefficients in the fluid boundary layers that form on the membrane's feed and draw side, respectively [33]. For membranes with a thick and less porous support layer, the solute resistance to diffusion in the support layer $1/k_M$ is dominant, and is given by [34]:

$$\frac{1}{k_M} = \frac{S}{D} \tag{9}$$

where D is the diffusivity of the solute.

2.2. Membrane characterization at a discrete operating pressure

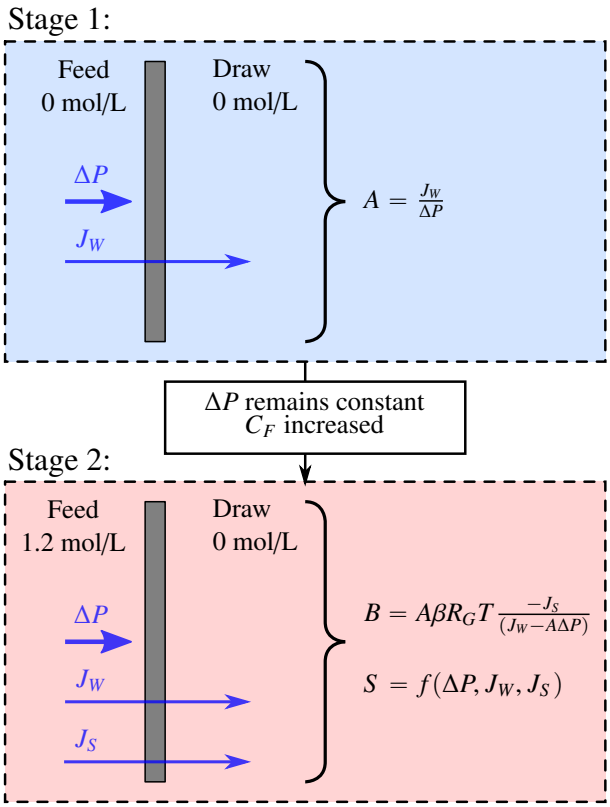

Figure 2: The integrated two-stage ABS method to determine the membrane properties at a discrete operating pressure.

The experimental and numerical procedure to determine the membrane properties at a given operating pressure using the integrated two-stage ABS method are shown in figure 2.

2.2.1. Stage 1: Determining A

The steady-state water flux is recorded for the specified operating pressure with both the feed and draw solution being deionised. Under these conditions, A can be exactly calculated, as equation (2) reduces to:

$$A = \frac{J_W}{\Delta P} \tag{10}$$

with A being the only unknown in equation (10). Its approximation can be improved by increasing the total number of steady-state measurements n of J_W at relatively constant ΔP. Hence, an increase in n lowers the influence of experimental outliers caused by minor inaccuracies (e.g. pressure fluctuations due to pump and valve vibrations) on the approximation of A. A can either be approximated by using the median calculation approach:

$$A^{MED} = median\,(J_{W,i}/\Delta P_i)_{i=1}^{n} \tag{11}$$

or by minimising the error of the over-determined system using least-squares regression (LSR):

$$Err_A = \sum_{i=1}^{n}\left(\frac{J_{W,i}}{\Delta P_i} - A^{LSR}\right)^2 \tag{12}$$

$J_{W,i}$ and ΔP_i are the measured water flux and transmembrane hydraulic pressure for each steady-state measurement i.

2.2.2. Stage 2: Determining B and S

In the second stage of the experiment, either the feed (or draw) solute concentration is raised by adding a known amount of NaCl. In this study, a 1.2 M feed solution is utilized for the reasons stated in section 2.4.2. Once J_W and J_S stabilize, these can be recorded to determine B and S.

For the indicated directions of J_W, J_S and ΔP for HPRO and OARO in figure 1, B can be calculated by rearranging equation (3) to give [31]:

$$B = A\beta R_G T\frac{-J_S}{(J_W - A\Delta P)} \tag{13}$$

The main benefit of using the ORF model is that B and S are decoupled from each other. In equation (13), B is decoupled from S, as the terms representing concentration polarisation are not present in equation (13). Thus, B is the only unknown in equation (13) and can be directly determined. Similarly as to the approximation of A, more steady-state measurements of J_W and J_S at ΔP lead to a better approximation of B, which can either be calculated using:

$$B^{MED} = median\left(A^{MED}\beta R_G T\frac{-J_{S,i}}{(J_{W,i} - A^{MED}\Delta P_i)}\right)_{i=1}^{n} \tag{14}$$

or by minimising the error:

$$Err_B = \sum_{i=1}^{n}\left(A^{LSR}\beta R_G T\frac{-J_{S,i}}{(J_{W,i} - A^{LSR}\Delta P_i)} - B^{LSR}\right)^2 \tag{15}$$

With A known, S can be determined independently of B using either the median or LSR calculation approach. The only unknowns remaining in equation (2) are f_{DCP} (which contains k_D and S) and f_{CCP} (which contains k_F). Both k_F and k_D can be estimated using the Sherwood number Sh knowing the given channel geometries and crossflow velocities [35]. No spacer is used in the feed channel and assuming turbulent flow (Reynold's number $Re > 2000$), k_F is calculated using:

$$k_F = Sh_F D/d_H \tag{16}$$

where d_H is the hydraulic diameter of the feed channel and Sh_F is [36]:

$$Sh_F = 0.04\,Re^{0.75}Sc^{0.33} \tag{17}$$

where Sc is the Schmidt number. Similarly, k_D can be calculated using the hydraulic diameter of the draw channel and the Sherwood number. In this case, the draw channel contains spacers and hence, Sh_D is given by [37]:

$$Sh_D = 0.0096\, Re^{0.5} Sc^{0.6} \tag{18}$$

With k_F and k_D calculated, S is the only remaining unknown in equation (2). Using the median approach, S is given by:

$$S^{MED} = median\left(D\left(1/k_{DCP,i} - 1/k_D\right)\right)_{i=1}^{n} \tag{19}$$

where $1/k_{DCP,i}$ is:

$$1/k_{DCP,i} = -\log(1 - f_{DCP,i})/J_{W,i} \tag{20}$$

and f_{DCP} is determined by rearranging equation (2).

On the other hand, S can also be determined by minimising the error Err_S using LSR:

$$Err_S = \sum_{i=1}^{n} \left(J_{W,i} - J_{W,i}^{LSR}\right)^2 \tag{21}$$

where $J_{W,i}$ is the measured water flux for each steady-state measurement i and J_W^{LSR} is calculated using equation (2) with S being the only unknown. All other variables in equation (2) are either continuously measured, such as π_F, π_D, J_S and ΔP, or have already been determined (e.g., A, k_F and k_D).

2.3. Membrane characterization over a wide pressure range

As laid out in section 2.2, A, B and S can be determined using either the median or the LSR calculation approach for each pressure stage being investigated. Moreover, the integrated two-stage (ITS) ABS method is also easily scaleable to a range of operating pressures to determine how the membrane's intrinsic properties change with ΔP. Figure 3 shows how the membrane can be characterized over a wide range of operating pressures using either 1) two experiments and two uncompressed membrane coupons (figure 3a), or using 2) a single experiment with a single membrane coupon (figure 3b).

The first experimental method (figure 3a) is employed to determine the membrane's A, B and S values over the desired pressure range in section 4.1. This method is simpler and faster if many pressure stages are investigated, as no feed and draw solutions need to be changed during each of the individual pressure stages. However, this approach can be problematic in that minor defects or differences between the membrane coupons can affect the determined A, B and S values.

As shown in figure 3a, A is firstly determined for each investigated pressure stage using deionised feed and draw solutions. After A has been determined for each pressure stage, the compressed membrane coupon is replaced with a new, uncompressed one and the experiment is repeated. However, a saline feed (or draw) solution is now used so that B and S can be calculated.

Alternatively, figure 3b shows how the membrane can be characterized over a wide pressure range using only one membrane coupon and in a single experiment. The results in section 4.3 were obtained using this experimental approach. It was chosen for the increased-decreased compression cyclic tests as only a few pressure stages were investigated.

For the first pressure stage, A is firstly determined using deionised feed and draw solutions. Thereafter, a saline solution is added to the feed or draw stream to determine B and S at constant ΔP. Once enough steady-state measurements have been taken to accurately determine A, B and S for the first pressure stage, ΔP can be adjusted. At the new pressure stage, the water and solute flux can then be measured without altering the draw and feed solutions to determine B and S. The saline solution can then be drained, the channel flushed and the solutions replaced by deionised water so that A can be calculated for the same ΔP. The membrane coupons were not removed from the test cell for rinsing, as channel flushing was sufficient to minimise the salinity within the system. This can be done without changing the membrane's characteristics as ΔP remains unchanged. This process can then be repeated for any number of desired pressure stages and hence offers a quick, accurate and robust approach to determine A, B and S for each ΔP.

In either case, having J_W and J_S measurements for a range of ΔP allows the investigator to not only determine discrete A,B and S values, but to also determine a functional relationship between the membrane properties and ΔP. For example, each membrane property can be represented by an m-th order polynomial of ΔP, where the unknown coefficients can be determined using the LSR approach:

$$\begin{aligned} A^m &= a_1\Delta P_i^m + a_2\Delta P_i^{m-1} + ... + a_m\Delta P_i + a_{m+1} \\ Err_A &= \textstyle\sum_{i=1}^{n}\left(\frac{J_{W,i}^{EXP}}{\Delta P_i^{EXP}} - A^m\right)^2 \end{aligned} \tag{22}$$

$$\begin{aligned} B^m &= b_1\Delta P_i^m + b_2\Delta P_i^{m-1} + ... + b_m\Delta P_i + b_{m+1} \\ Err_B &= \textstyle\sum_{i=1}^{n}\left(A^m\beta R_G T\frac{-J_{S,i}}{(J_{W,i}-A^m\Delta P_i)} - B^m\right)^2 \end{aligned} \tag{23}$$

$$\begin{aligned} S^m &= s_1\Delta P_i^m + s_2\Delta P_i^{m-1} + ... + s_m\Delta P_i + s_{m+1} \\ Err_S &= \textstyle\sum_{i=1}^{n}\left(J_{W,i} - J_{W,i}^m\right)^2 \end{aligned} \tag{24}$$

2.4. Practical guidance for the proposed characterization method

2.4.1. A, B and S of membrane-spacer combinations

In existing membrane characterization approaches, the transport and structural properties of the membrane system are assumed to be solely dependent on the membrane's active layer and support layer properties. However, deformation of the whole module during operation is expected to affect the membrane's intrinsic properties and specifically the parameters A, B and S. For example, if a more open spacer backing is chosen for the same membrane, then membrane deformation will be more severe and the changes of A, B and S will be more pronounced with an increase in the operational pressure ΔP [18]. One of the main advantages of the integrated two-stage ABS method is its suitability to determine the transport and structural properties of the entire membrane module, which not only includes the membrane but also its entire support structure. This is beneficial for the design of osmotically- and pressure-driven

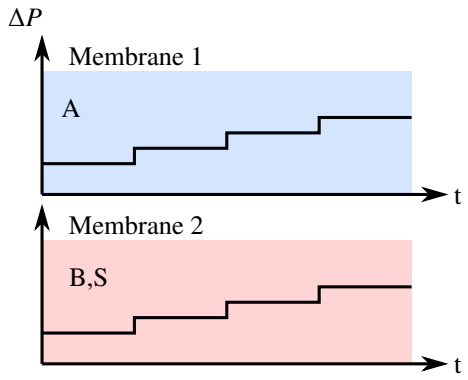

(a) In the first experiment A is determined for each pressure stage using an uncompressed membrane coupon and deionized feed and draw solutions. Secondly, the experiment is restarted using a new, uncompressed membrane coupon to determine B and S for each pressure stage by employing a saline feed (or draw) solution.

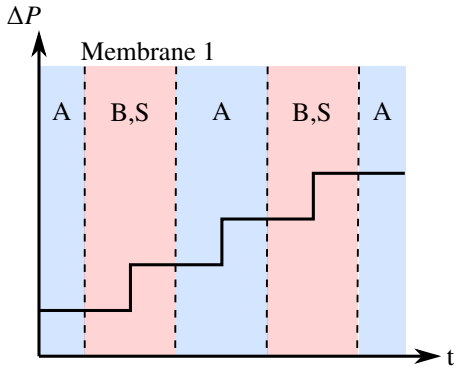

(b) A single experiment, using a single membrane coupon, is required to determine the membrane's intrinsic properties over several pressure stages. The blue shaded time intervals indicate the periods in which deionised water is used to determine A. In the red intervals, the deionised feed or draw solution is replaced by a saline solution at constant ΔP so that B and S can be determined.

Figure 3: Two experimental approaches to determine the membrane properties over a wide pressure range using the integrated two-stage ABS method.

membrane modules. Ideal membrane-spacer combinations can then be determined to improve the process performance by minimising membrane deformation, pumping costs etc. Using the ITS ABS method, it is possible to easily test various membrane-spacer combinations in a membrane cell and determine how A, B and S change with ΔP. In addition, an entire membrane module can also be tested using the proposed method to determine the overall transport and structural properties of the module. This possibility is discussed in greater detail in section 4.4.

2.4.2. *Accuracy and robustness of the median and LSR approach*

In cases of dilutive internal concentration polarisation (DICP), an important consideration has to be made when determining S. As shown by equation (6), the exponential term representing DICP rapidly approaches zero for thicker membranes at higher water fluxes. Consequently, as f_{DCP} approaches 1 (figure 4) at relatively high experimental water fluxes, it becomes impossible to extract and accurately determine S from the experimental findings, as the influence of S on J_W and J_S diminishes with higher J_W. The pressurized solution therefore needs to be more concentrated to increase the feed osmotic pressure and reduce the experimental water flux. In this study, the feed solution is pressurized up to 60 bar and a 1.2M NaCl solution is utilized to limit the maximum water flux to below 15 $L/(m^2h)$ (LMH).

2.4.3. *Numerical error incurred by assuming the osmotic coefficient is constant*

In the ORF model, it is assumed that the solution is ideal and that the van't Hoff factor in equation (4) remains constant. This assumption may, however, lead to the overestimation of the osmotic pressure of the solution at high concentrations. The van't Hoff factor β is given by:

$$\beta = i\phi \tag{25}$$

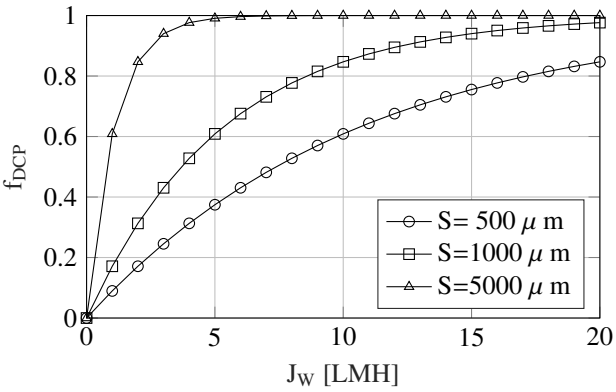

Figure 4: Internal concentration polarisation factor of the draw solution with respect to the water flux for three different structural parameters.

where i is the number of dissociating ions (e.g. 2 for NaCl) and ϕ is the osmotic (or activity) coefficient, which is actually dependent on the solution concentration, as shown in figure 5 [38]. As mentioned in section 2.4.2, to determine B and S in this study, a 1.2M NaCl feed solution is utilized, which means that ϕ of the actual feed solution is 3.14% higher than that for an ideal, dilute feed solution. This small error may affect the B and S values determined using the median and LSR calculation approach.

Utilising even higher concentration feed or draw solutions to determine B and S will lead to an increase in this error, as shown in figure 5. However, higher concentration feed solutions are only required in order to limit the water flux for highly permeable membranes operated at high ΔP and even then, other errors incurred during the experimental process (e.g., inaccurate measurements of the crossflow velocity, the operating pressure and the feed and draw concentrations using conductivity) may outweigh the error incurred by assuming ϕ as constant.

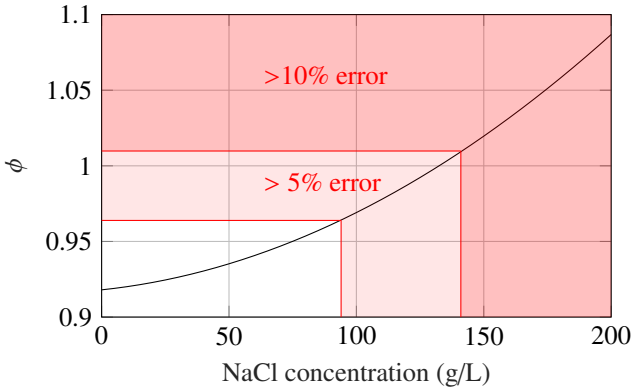

Figure 5: The change of the osmotic coefficient with the solution concentration. The red shaded boxes indicate the numerical error incurred when assuming that ϕ remains constant with the NaCl concentration relative to infinite dilution.

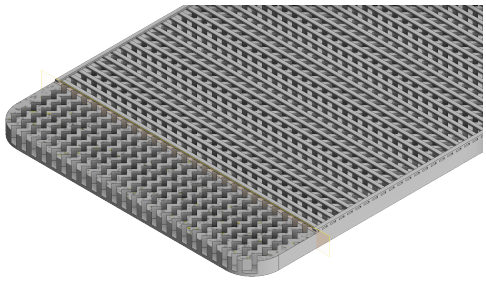

Figure 6: 3D printed spacer designed to support the RO permeate carrier and the membrane when used in the permeate channel within the membrane test-cell. The underlying pattern is revealed in the figure to exhibit the three-dimensional spacer shape designed to improve the flow turbulence while offering a rigid support for the membrane.

3. Experimental methodology

3.1. Membranes and spacer backing

Two commercially available membranes were used to develop and validate the ITS ABS method; both of them are suitable membranes for pressure- and osmotically driven membrane processes. The first investigated membrane is an aquaporin (AQP) based TFC membrane from Aquaporin A/S (Copenhagen, Denmark). This AQP TFC membrane has a thin substrate and was originally designed for use in forward osmosis processes. To investigate whether our proposed method is also applicable for the characterization of thicker membranes, a FilmTec flat-sheet brackish water RO membrane (BW30LE) was directly purchased from DuPont and tested. The membranes were stored at 4C and extensively rinsed and soaked in Milli-Q water for over 24 hours before use. All tested membrane coupons had an active membrane area of approximately 42 cm^2.

A 3D printed spacer (figure 6) coupled with a tricot-type RO permeate carrier, the latter obtained from a commercial RO spiral wound module [18], were placed in the permeate (draw) channel of the membrane test cell. This spacer combination in the permeate (draw) channel could fully support the membranes at operating pressures of up to 60 bar when operated in RO mode. The 3D printed spacer was produced from polylactic acid (PLA). PLA prints have a good dimensional accuracy, which allows for an intricate spacer design to enhance mixing and mass transfer in the draw channel while ensuring that the membrane is well supported. PLA is widely used for 3D printing because of its relatively low melting temperature and good mechanical strength and stiffness. To reduce the spacer openings, the RO permeate carrier was placed on top of the 3D printed spacer to further improve the membrane's support structure. No feed spacer was used in the membrane experiments to prevent its interference with the membrane's active layer.

3.2. Experimental procedure and chemicals

All solutions were prepared using ultrapure water and with ACS reagent grade sodium chloride, which was purchased from Sigma Aldrich. The membranes and spacer combination were tested in a membrane test cell (Sterlitech) that can withstand operating pressures of up to 69 bar. However, the digital pressure gauges were only calibrated for operating pressures of up to 60 bar, which was therefore set as maximum for all tests performed.

The test-rig is described in detail in Appendix A. No dosing pumps were utilized during the experiments to control the concentrations of the feed and draw solutions. Thus, the feed solution was concentrated and the draw solution diluted with the progress of each test. The changes in feed and draw concentration were constantly recorded and considered in the calculation of J_S and the membrane's intrinsic properties. The temperature of the pressurized feed solution was kept constant at 25 (plus/minus 0.5) C using a cooling coil.

For each investigated pressure stage, steady-state operation was reached after approximately 20-30 minutes. Once steady-state operation was achieved, J_S, J_W, ΔP and the feed and draw conductivities were recorded every 10 seconds for 10 minutes to ensure that enough measurements were available to determine the membrane's properties accurately.

3.3. The RO-FO characterization method

As a benchmark, the A, B and S values of the AQP and BW30LE membranes were also determined using the RO-FO method. In this study, the modified RO test is utilized to determine A and B, which was previously used by Kim and Elimelech [26] and She et al. [18]. In the modified RO test, a modification is made to the standard RO test so that a counter-current flow cell can be utilized by simply recirculating the permeate on the draw/permeate side while determining A and B. The chosen operating conditions for the modified RO-FO characterization method are given in table 1. As suggested by Cath et al. [21], no spacer is utilized in the feed channel.

Generally, A is determined at four different applied pressures (5, 10, 15 and 20 bar) and assumed constant with respect to ΔP using the RO-FO method [39]. The measured pure water fluxes are then plotted against ΔP, and hence A can be obtained from the slope of the fitted straight line (equation (10)). Similarly, the values of B and S are also assumed constant with respect

Table 1: Operating conditions for characterization of the AQP and BW30LE membranes using the RO-FO method.

Testing mode: RO for determination of A	
Membrane orientation	AL-FS
ΔP	5,10,15,20 bar
C_F	0 M
C_D	0 M
Cross-flow velocity	0.1 m/s
Testing mode: RO for determination of B [40]	
Membrane orientation	AL-FS
ΔP	10 bar
C_F	2 g/L NaCl
C_D	0 M
Cross-flow velocity	0.1 m/s
Testing mode: FO for determination of S [21]	
Membrane orientation	AL-FS
ΔP	0 bar
C_F	0 M
C_D	1 M
Cross-flow velocity	0.1 m/s

to the applied pressure and are determined at 10 bar and 0 bar, respectively.

4. Results and discussion

4.1. Membrane characterization over a wide pressure range

In this section, the integrated two-stage ABS method, as well as the modified RO-FO method are used to characterize the AQP and BW30LE membranes. The membranes were characterized using uncompressed membrane coupons to show the effect of membrane compression itself on its intrinsic properties.

Regarding the modified RO-FO characterization test, an uncompressed membrane coupon was used for each of the three tests required to determine A, B and S. The tests were performed under the conditions specified in section 3.3. On the other hand, two uncompressed membrane coupons were utilized to characterize the membrane using the ITS ABS method (figure 3a). The first uncompressed membrane coupon was used to determine A over a 5-60 bar pressure range, using deionised feed and draw solutions. Afterwards, B and S were determined for the same pressure range using the second uncompressed membrane coupon using a 1.2 M NaCl feed solution.

Figure 7 shows the obtained A, B and S values for the AQP (left column) and BW30LE (right column) membranes. Each membrane parameter is calculated using either 1) the modified RO-FO method, 2) the median (MED) or 3) the LSR calculation approach to determine the membrane's intrinsic properties at each distinct operating pressure, or using 4) the global LSR (GLSR) calculation approach to represent A, B and S as second order polynomials of ΔP.

As shown in figure 7, the median calculation approach offers reasonably accurate predictions of A and B, but this approach is inadequate to determine S. The median approach is susceptible to minor experimental inaccuracies, as S is analytically determined for each set of measurements i before determining the median. Therefore, small experimental inaccuracies cause severe numerical instabilities due to the highly nonlinear nature of equation (19). On the other hand, the LSR approach is more robust, as an approximate solution of S is directly determined by solving the over-determined system of all nonlinear equations i simultaneously. Furthermore, the GLSR calculation approach offers a smooth and reasonably good fit to the LSR results for the A, B and S values of both membranes.

The water and solute permeabilities determined using either characterization method coincide well at lower operating pressures for both the AQP and BW30LE membranes. This is to be expected, as both characterization techniques are performed at similar operating pressures so that the effect of membrane compaction and/or stretching on the membrane's intrinsic properties is comparable in both techniques. This is, however, not the case at higher operating pressures. The A and B values obtained using the ITS ABS method indicate that the water and solute permeability of both membranes decrease with an increase in the operating pressure. This suggests that membrane compaction and densification under the stress induced by the applied pressure dominate membrane deformation. However, localized membrane stretching is still observed, but to a lesser extent than observed in She et al. [18]. More open spacers were used to back the membrane in She et al. [18] and A and B were found to increase instead of decrease due to membrane stretching. Although permanent spacer intrusions were visible on the membrane coupon after the completion of the characterization tests and especially for the thinner AQP membrane, membrane compaction seems to dominate, as A and B decrease with the applied hydraulic pressure [8, 14, 41, 42]. The dominance of membrane compaction over stretching could be explained by the use of a rigid and dense spacer backing.

As shown in figure 7, the selectivity of both membranes increases with the applied hydraulic pressure (B/A reduces with ΔP). Similar findings were made by Pendergast et al. [43] and by Ng et al. [44]. In the former studies, it was argued that compaction of the support layer will lead to the equal reduction of both the solute and water flux, as the flow resistance increases with both the reduction in substrate surface porosity and with pore tightening. While the densification of the support layer may lead to the reduction of both A and B, it does not explain why B decreases more drastically than A with the applied hydraulic pressure. Hence, Pendergast et al. [43] conclude that the increase in salt rejection may be a consequence of compaction affecting the thin membrane's active layer.

To explain the phenomenon of increased selectivity (B/A) with membrane compaction, the reader is referred back to the work of Yip and Elimelech [45]. Their findings indicate that TFC polyamide membranes exhibit a permeability-selectivity trade-off ($B \propto A^3$). This relationship holds for a variety of TFC polyamide membranes and is argued to be linked to a fundamental physical principle that governs transport across the membrane's active layer [45, 46]. Therefore, it could be reasoned that the improved membrane's selectivity at elevated ΔP is indeed associated with the compaction of the thin selec-

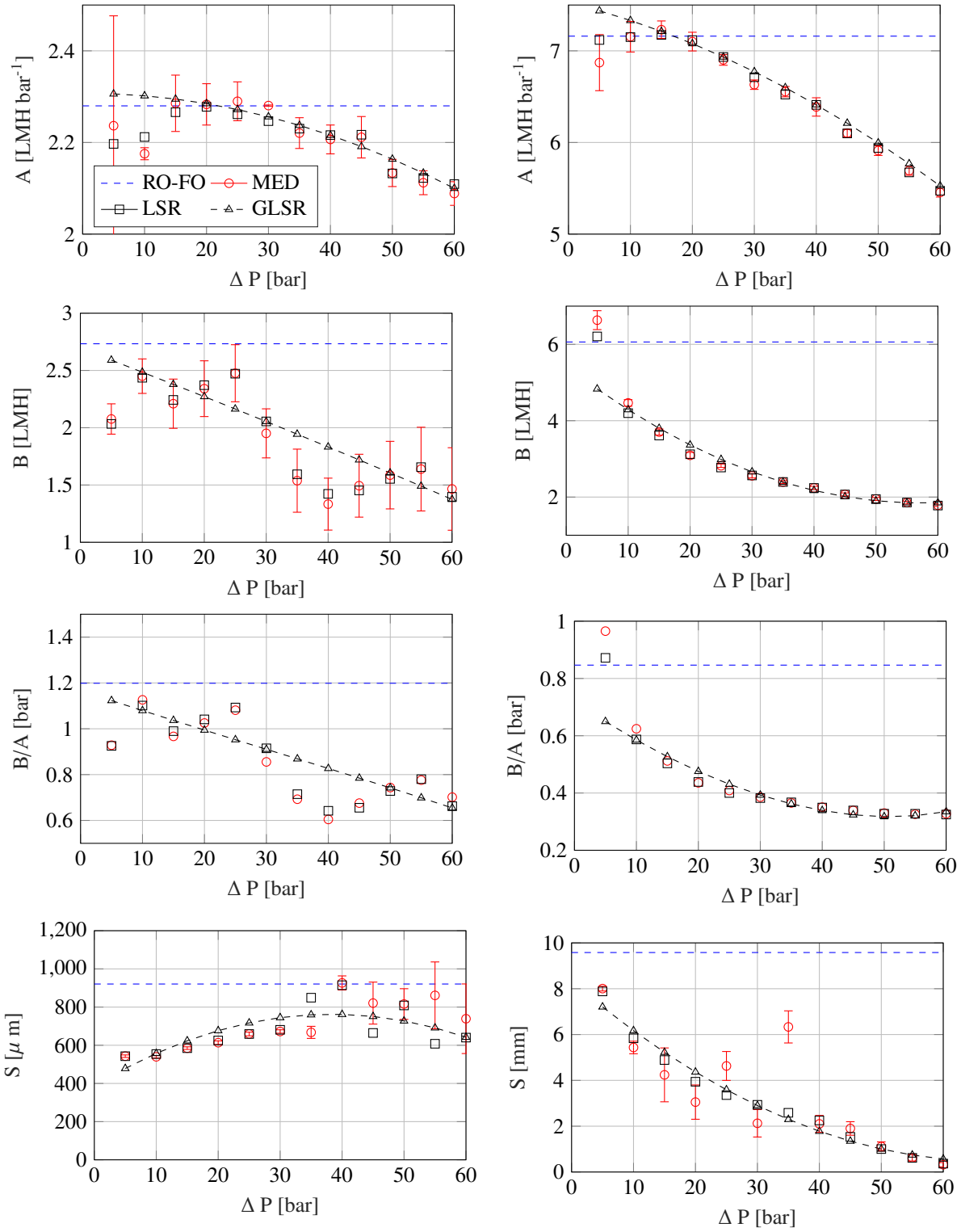

Figure 7: The determined A, B and S values for the AQP (left column) and BW30LE (right column) membranes over a wide pressure range.

tive polyamide layer and related to the permeability-selectivity trade-off presented by Yip and Elimelech [45]; in essence, selectivity increases as A decreases.

While the water and solute permeance follow similar trends for both membranes, the change of S with ΔP seems to differ more widely between the two. According to the LSR and GLSR results, the structural parameter of the AQP membrane first increases slightly with ΔP and then slowly declines once ΔP exceeds 40 bar. The overall change in S of the AQP membrane is approximately 300 μm, which is a significant change when con-

sidering that the overall structural parameter varies between 500 μm and 800-900 μm. Compaction of the support layer at higher applied pressures can lead to significant structural changes of the membrane structure, and may affect the void volume, noting that the FO membrane substrate is even more porous than the RO membrane substrate. However, a standard deviation of more than 200 μm has been recorded in other studies for commercial or hand-cast, thin FO membranes and may hence be caused by minor measurement inaccuracies or membrane defects/variabilities [47, 21, 48].

Similarly, the change in S for the BW30LE membrane is significant. With an increase in ΔP, S reduces from 8 mm (5 bar) to less than 2 mm (60 bar). This suggests that membrane compaction reduces the thickness (and perhaps the tortuosity) of the BW30LE support layer while the membrane pores may also be enlarged due to localized tensile stretching [17]. Similar findings were reported by She et al. [17] and She et al. [18], who found that the structural parameter of both cellulose triacetate (CTA) and TFC membranes can reduce with the applied pressure, especially with severe membrane deformation at high applied pressures and when more open spacer backings are employed. Contrary findings were reported by Madsen et al. [4], who reported that the S-value of a CTA FO membrane increases with the applied hydraulic pressure. Differences in the spacer support, membrane materials and hence the different mechanical properties of the overall membrane-spacer combination may explain the differences in the observed S trends for the BW30LE, AQP and CTA membranes.

In table 2, the determined A, B and S values are compared to those presented in other studies. Firstly, it should be mentioned that Madsen et al. [4] reported that their investigated AQP membrane samples were too fragile for characterization. The AQP membrane burst pressure was reported as 10 bar, whereas the AQP membrane samples investigated in this study, which were also supplied by Aquaporin A/S (Lyngby, Denmark), could withstand operating pressures of up to 60 bar. Furthermore, in this study, the AQP membrane showed no signs of failure at 60 bar. Instead, the membrane properties improved with compaction at higher ΔP, as the membrane's selectivity increased while its structural parameter firstly increased and then decreased with ΔP. This discrepancy could be due to a multitude of factors, including the use of different; 1) spacer backings, 2) membrane test cells, 3) operating conditions, 4) characterization techniques, and 5) the use of membrane samples from different production batches.

As seen in table 2, large discrepancies between the reported A, B and S values are a common phenomenon, even though the same, or a similar, membrane type are being investigated. This not only makes it difficult to compare different membrane types but also complicates the design and modelling of membrane processes. To be able to offer more consistent and representative A, B and S values of membranes, it is important to understand the main causes for these inconsistencies:

Characterization methods: Tiraferri et al. [23] pointed out that the A, B and S values calculated using their single FO method did not correspond well to those obtained using the RO-FO method. This is because the FO membranes where once characterized under pressure (the RO-FO method) and once at ambient pressure (the single FO method). Similarly, Wong et al. [55] observed that during membrane characterization the CTA membrane suffered from plastic deformation at high pressures. Hence, the chosen characterization method significantly impacts on the obtained A, B and S values and their accuracy [47]. It is therefore difficult to compare the measured values for the membrane's intrinsic properties when these values were determined using different characterization methods.

Operating conditions: Differences in the operating conditions during characterization can significantly affect measurements of the membrane's intrinsic properties. Wong et al. [55] and McCutcheon et al. [56] observed that the calculated water permeability of cellulose-based polymeric FO membranes decreased with the solution concentration. This reduction in water permeability is associated with the de-swelling of the membrane at higher solution concentrations [57]. Furthermore, Wong et al. [55] reported that the calculated structural parameter was significantly higher at lower salt concentrations of around 10 g/L (S calculated as ≈ 500 μm) but remained relatively constant at salt concentrations exceeding 32 g/L (S calculated as ≈ 300 μm). As stated by McCurley and Seitz [58], membrane swelling depends on the difference between the ionic strength of the solution and the charge density of the polymer. Therefore, it is reasoned by Wong et al. [55] that beyond a certain solute concentration, the charge densities in the polymer can be neutralized and hence, membrane swelling is minimized as a result of the reduction of electrostatic repulsion between the polymer chains.

In addition to the solute concentration, the temperature and composition of the feed and draw solution were also found to significantly affect the membrane's structural parameter [59, 55]. Furthermore, the hydraulic [60, 4, 16] and osmotic [44] pressure significantly affect the membrane properties, as has become evident from this study and others. It can therefore be concluded that performing membrane characterizations under different and non-representative conditions can lead to erroneous estimations of the expected process performance. In comparison to other characterization techniques, using the ITS ABS method makes it possible to determine A, B and S at operating pressures, solution temperatures, concentrations and compositions that are closer to, or equivalent to, those of the actual process for which the membrane is intended for.

Membrane samples: As reported by several researchers, A, B and S can vary even when the same membrane type is investigated [60, 48, 49]. Hussain et al. [60] reasoned that the cause for the variation in water permeability between different membrane samples is most likely caused by variations in the morphology—surface roughness [61], pore size distribution [62], and thickness [63] of the membrane's active layer. As reported by Tang et al. [64], Tang

Table 2: Comparison of the obtained A,B and S-values for the AQP and BW30LE membranes with those stated in literature.

Characterization method [a]	A [LMH bar^{-}1]	B [LMH]	B/A [bar]	S [μm]	Reference
Aquaporin membranes [b]					
LSR (10 bar)	2.21	2.44	1.10	557	This work
LSR (50 bar)	2.13	1.56	0.73	809	This work
Modified RO-FO	2.28	2.73	1.20	921	This work
Modified RO-FO	N/A [c]	N/A [c]	N/A [c]	N/A [c]	[4]
Standard RO-FO	0.52	0.09	-	444-825	[48]
Standard RO-FO	3.03	1.76	0.58	710	[49]
Standard RO-FO	2.09	0.07	-	301	[50]
Standard RO-FO [d]	3.1	0.9 (KCl)	-	735	[51]
FO [d,e]	6.60	1.70	0.26	420	[52]
BW30LE membranes					
LSR (10 bar)	7.15	4.20	0.58	5836	This work
LSR (50 bar)	5.94	1.90	0.33	1115	This work
Modified RO-FO	7.16	6.06	0.85	9580	This work
A-B correlation [f]	6	2.87	-	10000	[45]
A-B correlation [f]	8	6.81	-	10000	[45]
Standard RO-FO	2.79	1.20	0.47	14000	[53]
Standard RO-FO	3.67	0.59	-	-	[54]

[a] The standard and modified RO-FO method are described in Cath et al. [21] and Kim and Elimelech [26], respectively.
[b] All aquaporin FO membranes were purchased from Aquaporin A/S (Lyngby, Denmark) unless otherwise stated.
[c] The investigated AQP membranes were too fragile for characterization and had a burst pressure of 10 bar.
[d] AQP based polyamide TFC-FO membranes supplied by Aquaporin Asia (Singapore).
[e] The FO characterization technique is laid out by Tiraferri et al. [23].
[f] Yip and Elimelech [45] developed an equation that correlates the permeance and selectivity of polyamide membranes.

et al. [65] and Kim et al. [62], the membrane properties are affected by the synthesis conditions of the membrane's active layer (and also its support layer). Therefore, the variations in membrane properties can be caused by minor differences and production changes between membrane batches.

Calculation approach and measurement equipment:
Membrane characterization methods are prone to numerical and experimental errors. As discussed in this section, the LSR and GLSR calculation approach are preferred over the median approach to minimise numerical instabilities and inaccuracies. Tiraferri et al. [23] also used the LSR approach and stated that a minimum of 4 tests at different concentrations are required to accurately determine A, B and S. In this study, A is determined independently of B and S while B is also decoupled from S. Hence, when using the ITS ABS method and the LSR calculation approach, only two tests (Refer to section 2.2) are required to accurately determine the membrane's intrinsic properties at any given operating pressure.

However, just like any other membrane characterization method, the proposed method in the current work is also prone to experimental errors that can be caused by, for example, system vibrations, erroneous readings or by faulty sensor calibrations. In appendix Appendix B, a sensitivity analysis is performed to show how erroneous measurements influence the A, B and S results. It is worthy of note that S is especially sensitive to the feed salinity (at higher ΔP), whereas S is relatively insensitive to erroneous feed and draw flowrate measurements.

All of these potential causes offer plausible explanations, to some extent, of the inter-laboratory variations in the reported membrane properties. While the structural parameter of the BW30LE membrane correlates well to those presented in literature at low operating pressures [66, 45, 53], the significant reduction of S with ΔP was unexpected. In other studies, S was always measured at close to ambient pressures; by extrapolation, the use of thicker membranes in osmotically driven membrane processes was always considered impractical. However, the sharp reduction in S of the BW30LE membrane with ΔP may make it, or similar membrane types, viable membrane choices for OARO, PAO or PRO.

From the LSR findings presented in table 2, the changes in the transport and structural parameters with ΔP are more severe for the BW30LE membrane than for the AQP membrane. For the BW30LE membrane, the respective changes of A, B and S are -16.9%, -54.8% and -80.9% when the applied pressure increases from 10 bar to 50 bar. On the other hand, the AQP A, B and S values change by -3.6%, -36.1% and +45.2% over the same pressure range. The BW30LE membrane is therefore more susceptible to compaction, which may be explained by its

relatively higher permeability/porosity. Similar to the findings presented in this study, Hussain et al. [60] found that membrane samples with an initially higher permeability were more susceptible to compaction. This trend can be explained by the fact that the membrane's mechanical strength decreases with increasing porosity (i.e. permeability) [67, 68].

4.2. Method validation

In this section, the accuracy of the integrated two-stage ABS method and that of the modified RO-FO method are put to the test. Both membranes have been tested under various operating conditions that are representative of those in various pressure- and osmotically driven membrane processes. In each test, the experimental water flux J_W^{Exp} and solute flux J_S^{Exp} have been recorded for the different solution concentrations and the different pressure stages (5-60 bar). The A, B and S values that were presented in section 4.1 were then used to model the water flux J_W^{Calc} and solute flux J_S^{Calc} for the given operational conditions and compared to the corresponding experimental measurements in figure 8 and figure 9. The dashed line in the figures would indicate a perfect fit between the experimentally determined and calculated water and solute fluxes.

4.2.1. PAO validation case

The first validation that was performed was to test both membranes under PAO conditions (C_F= 0 M, C_D= 0.6 M). For this test, the experimental and modelled water flux are compared in figure 8a and figure 8b. The modelled water fluxes, using either characterization method, correlate well with the experimental results at low operating pressures (i.e. at low water fluxes). However, at high operating pressures the calculated water flux, using the modified RO-FO method, diverges from the experimental values, especially for the BW30LE membrane. On the other hand, the ITS ABS method can accurately predict the water flux at any given pressure, even though the membrane's intrinsic properties were actually determined with completely different solution concentrations (A: C_F= 0 M, C_D= 0 M; B and S: C_F= 1.2 M, C_D= 0 M).

4.2.2. PRO and RO validation case

In this validation case, the feed concentration was chosen to be comparable to that of seawater while deionised water was used as draw solution (C_F= 0.6 M, C_D= 0 M). At low operating pressures, the effective osmotic pressure of the feed solution exceeds ΔP and hence, the process is PRO and J_W is negative (i.e. from draw to feed) for the AQP membrane (see figure 8c). In contrast, the water flux of the BW30LE membrane remains above zero for all pressure stages due to its thick support layer preventing a reverse water flux due to severe ICP (see figure 8d). The magnitude of all computed water fluxes are slightly greater than the experimental water flux during PRO operation for the AQP membrane, but during RO operation the water flux is accurately predicted using both characterization methods. For the BW30LE membrane, the water flux is overestimated at higher ΔP. However, the MED, LSR and GLSR predicted water fluxes are more accurate than those predicted using the modified RO-FO method.

Figure 9a and figure 9b compare the modelled and experimental solute fluxes for the PRO and RO validation case. As shown, the solute flux of the AQP membrane is under- and over- predicted using the ITS ABS method and the modified RO-FO method, respectively. The solute flux of the BW30LE membrane is, however, accurately predicted using the ITS ABS method whereas the modified RO-FO method significantly overestimates the solute flux at high operating pressures.

4.2.3. OARO validation cases

Two different OARO scenarios were investigated for validation purposes. The results of the first OARO test, with a 0.6 M feed and draw solution, are shown in figure 8e and figure 8f while the results of the second OARO test, with a 1.2 M feed and draw solution, are shown in figure 8g and figure 8h. In both validation cases, the AQP water flux is slightly underestimated at low operating pressures, but accurately predicted at higher ΔP (except using the MED calculation method). Similarly, the achievable BW30LE water flux is underestimated at low operating pressures, but slightly overestimated at higher ΔP when C_F= 0.6 M, C_D= 0.6 M. For the BW30LE membrane, the LSR and GLSR predicted values coincide better with the experimental values than those predicted using the modified RO-FO approach, especially at higher operating pressures.

In summary, the values obtained using the modified RO-FO method coincide well with the experimental values at low operating pressures. However, at high operating pressures the superior accuracy of the newly proposed method becomes evident, and it is therefore possible to determine the membrane's intrinsic membrane properties over a wide range of pressures, which is not possible using the conventional or modified RO-FO method. It is concluded that the newly proposed method in combination with the LSR or GLSR calculation approach offered reliable predictions, independent of the operating conditions. The results presented in this section demonstrate that the ITS ABS method can be utilized for the accurate and fast characterization of membranes intended for HPRO, OARO, PAO and PRO.

4.3. Increased-decreased compression cyclic testing

In addition to the tests presented in section 4.1 and section 4.2, both membranes were also characterized under cyclic conditions in which ΔP was varied between 10 and 50 bar in each of the three cycles. The results of the increased-decreased compression tests are presented in figure 10 and demonstrate the elastic and plastic behaviour of the membrane's properties.

For these cyclic tests, a single membrane coupon was used for membrane characterization and tested according to the experimental procedure shown in figure 3. This differs to the experimental approach followed in section 4.1 where one uncompressed membrane coupon was used to determine A and another one was used to determine B and S.

Figure 10 shows the cyclic A, B and S values that were calculated using the LSR and median approach. Furthermore, the non-cyclic A, B and S values (from section 4.1) that were calculated using the modified RO-FO method and the LSR approach

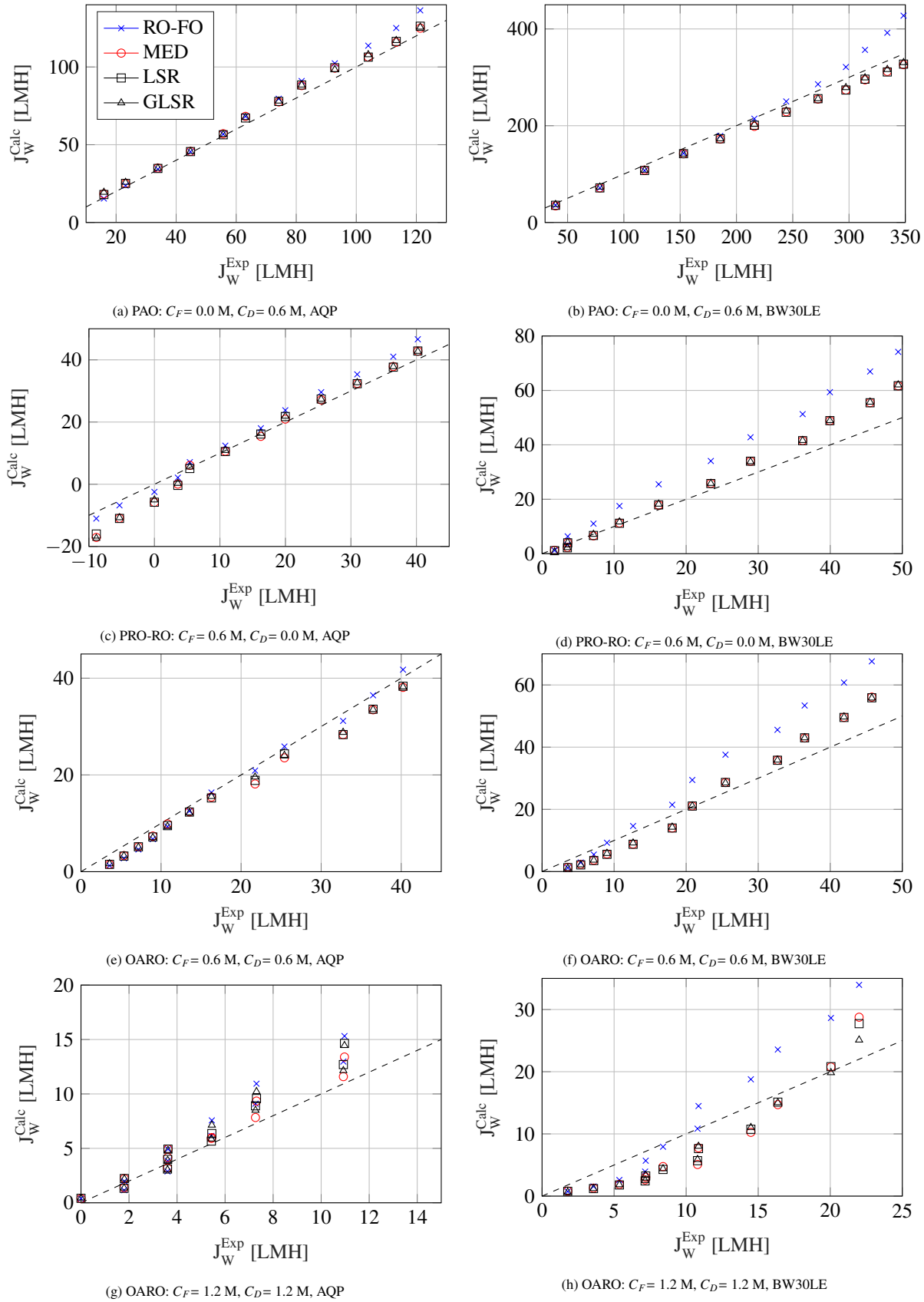

(a) PAO: C_F= 0.0 M, C_D= 0.6 M, AQP

(b) PAO: C_F= 0.0 M, C_D= 0.6 M, BW30LE

(c) PRO-RO: C_F= 0.6 M, C_D= 0.0 M, AQP

(d) PRO-RO: C_F= 0.6 M, C_D= 0.0 M, BW30LE

(e) OARO: C_F= 0.6 M, C_D= 0.6 M, AQP

(f) OARO: C_F= 0.6 M, C_D= 0.6 M, BW30LE

(g) OARO: C_F= 1.2 M, C_D= 1.2 M, AQP

(h) OARO: C_F= 1.2 M, C_D= 1.2 M, BW30LE

Figure 8: A comparison of the modeled and experimental data using the integrated two-stage ABS method and the existing RO–FO protocol, for different PAO, PRO-RO and OARO test cases. The dashed line would indicate a perfect fit between the experimentally determined water flux J_W^{Exp} and the calculated water flux J_W^{Calc}.

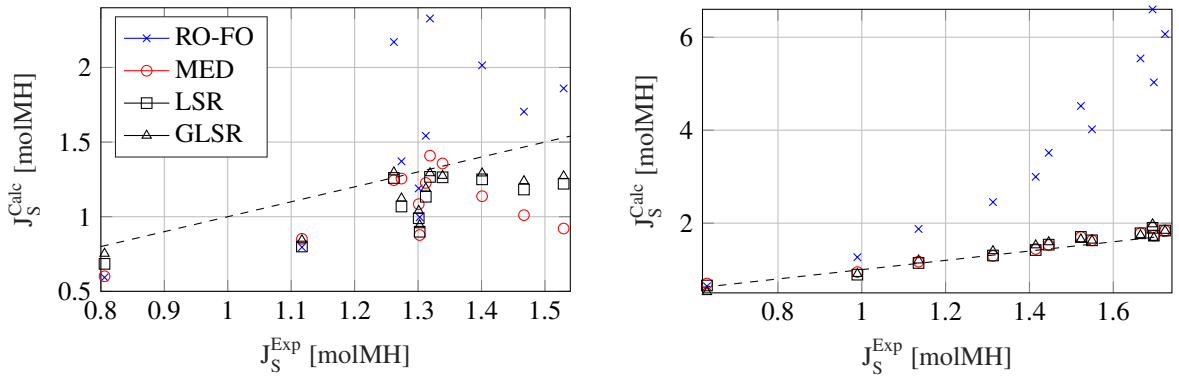

(a) PRO-RO: C_F = 0.6 M, C_D = 0.0 M, AQP

(b) PRO-RO: C_F = 0.6 M, C_D = 0.0 M, BW30LE

Figure 9: A comparison of the modeled and experimental data using the methodology proposed in this work and the existing RO–FO protocol, for different PRO-RO test cases. The dashed line would indicate a perfect fit between the experimentally determined solute flux J_S^{Exp} and the calculated one J_S^{Calc}.

are also shown in the figure. In the first cycle (C1) these results are comparable, as the membranes are initially uncompressed, whereas in the second (C2) and third (C3) cycle the membrane will be pre-compressed from the previous cycle.

From the figure, it can be seen that in the first cycle, the cyclic results generally differ from the non-cyclic ones at 10 bar (C1-10) but the two tend to converge at 50 bar (C1-50). These discrepancies may originate from the different experimental approaches, as laid out in section 2.3. On the one hand, the AQP and BW30LE membrane were characterized using two uncompressed membrane coupons during each non-cyclic test, whereas A, B and S were determined using a single membrane coupon during the cyclic tests. Furthermore, the membranes were initially compressed at 5 bar prior to being compressed at 10 bar during the non-cyclic tests (data adopted from figure 7) but directly compressed at 10 bar during the cyclic tests. Hence, the different compression routes may be another cause for the differences in the recorded A, B and S values at 10 bar.

In addition, similar findings were also made by Hussain et al. [60], who reported significant water flux variations between different NF-90 membrane samples at low operating pressures. On the other hand, the variation of the water flux reduced significantly with higher applied hydraulic pressures. Hussain et al. [60] argued that the non-uniformity of the active layer of TFC membranes are responsible for the large variations in the experimental results at low ΔP. This is because differences in the surface morphology, roughness and porosity of membrane samples directly affect the membrane's permeability according to the free volume theory [69]. However, the SEM results presented by Hussain et al. [60] show that during compaction, the membrane surface becomes smoother and has fewer, smaller holes. This change in surface structure with compaction may result in a higher degree of uniformity between membrane samples and hence may explain why the results of the cyclic and non-cyclic test converge at higher ΔP.

As observed by Hussain et al. [60], samples with a higher permeability experience higher flux reduction due to compaction. This is also observable in the A and B results presented in figure 10. Initially, A and B of the AQP membrane sample, which was used for the non-cyclic test, are higher and decrease with compaction. On the other hand, the initial water permeability of the AQP membrane sample used for the cyclic test is significantly lower and actually increases with compaction. Similarly, B of the cyclic AQP membrane sample slightly increases with compaction. For the BWRO membrane samples, the reduction of A and B is more pronounced with compaction for the samples with higher initial permeabilities. These findings support the hypothesis presented by Hussain et al. [60]; namely, that the membrane's permeability and compaction behavior are strongly dependent on the initial sample characteristic and its active layer properties.

After membrane compression in the first cycle, both membranes show signs of plastic deformation, as the A and B values do not return to their original states in the subsequent cycles. In the subsequent cycles, changes in A and B are less pronounced with increased and decreased compression. These findings correlate with those of Hussain et al. [60] who found that high pressure operation permanently deformed the membrane's active layer. A different finding was presented by Chen et al. [70], where membrane compaction was found to be reversible and that A/B remained constant after increased and decreased compression. However, the maximum investigated pressure was limited to 27.6 bar in that study whereas the maximum cyclic pressure investigated in this study was 50 bar.

While changes in A and B are less pronounced with increased and decreased compression after initial compaction, pronounced changes in S with ΔP are still observable for the BW30LE membrane. Based on these findings, it can be hypothesized that the active layers of both membranes are plastically deformed while their substrates are also plastically deformed (AQP membrane) or behave in a more elastic or sponge-like manner with minimal signs of plastic deformation (BW30LE membrane). Contrary to our findings, Kim et al. [71] reported a minimal permanent change in the S-value of two thin FO membranes that were compressed at pressures of up to 50 bar and then decompressed again. However, Kim et al. [71] developed a special PRO membrane test cell to minimise membrane deformation and hence concluded that plastic deforma-

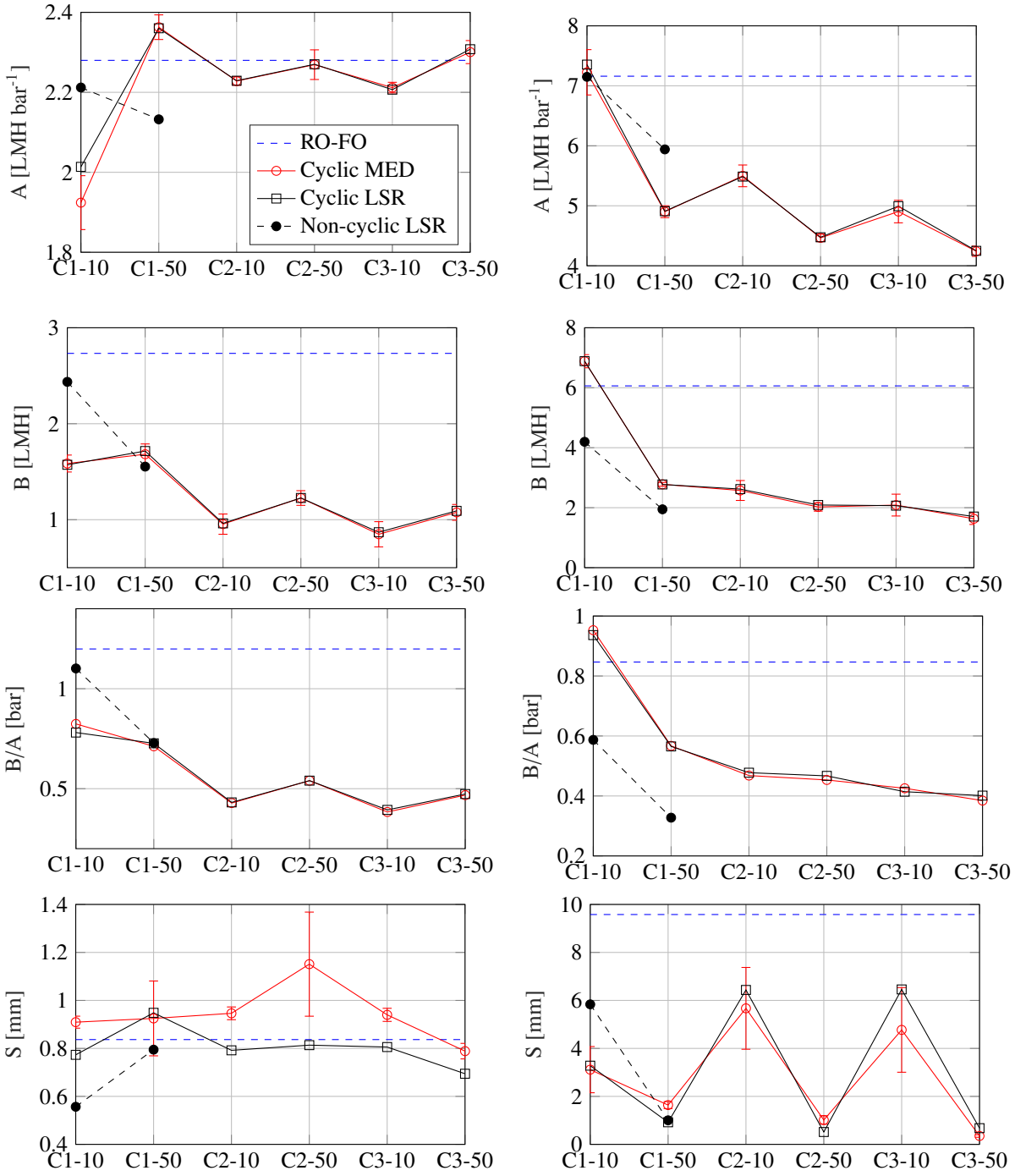

Figure 10: The cyclic variation of A, B and S values for the AQP (left column) and BW30LE (right column) membranes. ΔP alternates between 10 bar and 50 bar in 3 cycles (C1-C3). For comparison purposes, the non-cyclic LSR results from section 4.1 are also shown in the figure.

tion of thin FO membranes can be prevented if they are well supported, even at high operating pressures. In contrast, Madsen et al. [4] reported both plastic and elastic changes of a CTA membrane with increased-decreased compression, and that S increased with ΔP. The behaviour of the membrane's support layer is also likely to be dependent on the spacer backing (Please refer to section 2.4.1). The RO permeate carrier and the 3D printed spacer are more susceptible to deformation than the rigid, porous steel spacer used by Madsen et al. [4] and hence, a better stress distribution throughout the membrane and spacer backing may result in the observed elastic behaviour of the membrane's structural parameter.

In terms of accuracy, the A and B values obtained using the LSR and median calculation approach are indistinguishable, but as stated in section 4.1, the median approach offers less accurate predictions of the membrane's structural parameter. It is also worth noting that the values obtained from the non-cyclic LSR and RO-FO approaches can significantly dif-

fer from those obtained using the cyclic LSR approach in the second and third increased-decreased compression cycle. This again demonstrates that the membrane should be characterized under representative operating conditions using the ITS ABS method with the LSR calculation approach.

4.4. Implications of proposed method

The integrated two-stage ABS method has been developed and tested for flat-sheet membrane coupons placed in a counter-current membrane test cell. However, in principle, this characterization approach can be used for the characterization of any membrane (hollow-fibre, tubular or flat-sheet), and even for the characterization of entire membrane modules at any given pressure (or over an entire pressure range).

For example, the average water permeability of the entire membrane module can be determined at a distinct operating pressure by using deionised feed and draw solutions. Afterwards, the feed salinity can be raised so that average B and S values can be calculated from the measured water and solute fluxes. This simple two test process therefore makes it possible to robustly and accurately characterize entire membrane modules under representative operating pressures. The ITS ABS method therefore allows research workers to optimize various membrane-spacer combinations and to improve upon current module designs. Furthermore, with this new characterization method, it is possible to better understand how the A, B and S of various membrane modules change with ΔP. This will help to improve upon the design and operation of pressure- and osmotically driven membrane processes to 1) lower the cost and energy consumption of the plant, 2) improve the lifetime of the membrane, and 3) maximise plant productivity.

5. Conclusions

In this study, a robust membrane characterization method is presented with which it is possible to accurately characterize membranes and potentially entire membrane modules, at any given operational pressure. In addition, the proposed method is quick and simple, as only two tests at different concentrations are required per investigated pressure stage. The ability to offer more accurate predictions of A, B and S with ΔP will enable other research workers to optimize pressure- and osmotically driven membrane processes as well as improve upon membrane and module designs.

An Aquaporin membrane and a BW30LE membrane were characterized and tested for validation purposes under various operating conditions common to those of pressure- and osmotically driven membrane processes. Several important findings were made that are summarized here:

- In terms of calculation approaches, the LSR and median calculation approach offer similar A and B results but differ significantly when determining the membrane's structural parameter. The LSR approach is more accurate and hence, is the preferred choice.
- The validation results indicate that the newly proposed method is more accurate than the conventional RO-FO method. This is especially true at higher operating pressures, where membrane deformation significantly affects the membrane's intrinsic properties. This improved accuracy can mainly be attributed to the fact that the membrane is characterized under more representative operating conditions using the ITS ABS method.
- As shown in the presented results, A, B and S are significantly affected by membrane deformation, and especially at higher operating pressures. In agreement with other membrane compaction studies, the results indicate that the selectivity (B/A) of both the AQP and BW30LE membranes can be improved with increasing ΔP due to increased compaction.
- The initial membrane conditions and the active layer properties affect the membrane's permeability and compaction behaviour. More porous and permeable membranes experience a higher degree of compaction with ΔP. This finding is in line with results presented in other membrane compaction studies.
- The increased-decreased compression cyclic test results for the AQP membrane indicate that the membrane's active layer shows signs of plastic deformation after initial compaction. In contrast, the BW30LE membrane substrate is more elastic as S continues to oscillate with each increased-decreased compression cycle.
- Lastly, the sensitivity analysis shows that in order to attain accurate characterization results, S is most sensitive to differences in the feed concentration and least sensitive to the feed and draw cross-flow velocity.

6. Acknowledgements

This research was supported by the Start-up Grant (SUG #002195-00001) for Q.She from Nanyang Technological University. C.D. Peters would like to thank the Singapore Membrane Technology Centre (SMTC) at the Nanyang Technological University (NTU) for hosting a four-month research stay to carry out this research. Furthermore, Professor Tony Fane is thanked for his valuable comments on this work. C.D. Peters and N.P. Hankins are also grateful to the University of Bahrain (in the Kingdom of Bahrain) for the award of a DPhil scholarship to C.D. Peters at the University of Oxford.

Appendix A. Schematic diagram of experimental setup

The experimental setup used in this study was adopted from the one reported in our previous PRO study with two minor modifications [30]. Firstly, no dosing pumps were utilized during the experiments to control the concentrations of the feed and draw solutions. Hence, the salinity of the feed and draw solution had to be continuously monitored to determine their concentration changes with operational time. Secondly, the feed

solution was pressurised in this study instead of the draw solution. The weight of the draw solution was continuously measured to determine the water flux. A schematic of the experimental setup is shown in figure A.11.

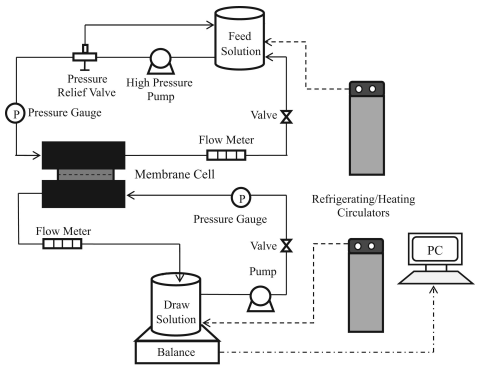

Figure A.11: Schematic of of experimental setup (modified from [30]).

Appendix B. Sensitivity analysis

Table B.3 lists the parameters upon which A, B and S depend and states their relationship to the variables present in equation (1) to equation (21). As shown by equation (10), A can be accurately determined if ΔP and J_W are correctly measured. J_W is calculated from the change of mass Δm of the draw tank over a given time period Δt using a digital scale. Incorrect pressure measurements indirectly affect A, whereas an incorrect reading of Δm directly affects A. It is important to note that if A is incorrectly determined, then this will directly affect the B and S results.

Table B.3: The relationship between the measured parameters and the dependent variables

Measured parameter	Dependent variable
ΔP	A, B, S
Δm	A, B, S, J_W, J_S
C_D, ΔC_D	B, S, J_S
C_F	S
Q_D	S, k_D
Q_F	S, k_F

In comparison to A, B and S are sensitive to a multitude of parameters. For B to be exact, the concentration of the draw solution and its change with time ΔS_D also need to be correctly measured, so that J_S is accurately calculated. S is also dependent on the feed concentration C_F and the flowrates of the feed Q_F and draw Q_D solutions. Q_F and Q_D are used to determine the cross-flow velocities in the feed and draw channel to accurately model ECP.

Figure B.12 shows the extent to which measurement inaccuracies affect the B and S values of the AQP membrane. The membrane's intrinsic properties were calculated using the ITS ABS method in combination with the LSR calculation approach.

As seen in the figure, B is relative insensitive to incorrect pressure measurements at higher ΔP, as a $\pm$ 1 bar difference becomes less significant. B is, however, more sensitive to incorrect Δm measurements, independently of the applied pressure. This is because an incorrect measurement of Δm affects a wide range of variables, which in turn affect B. Similarly, B is sensitive to the draw solute salinity, as B is directly related to J_S.

The membrane's structural parameter S is the most difficult to determine, due to the non-linearity of equation (2) and the dependency of S on all measured parameters. While the sensitivity of S remains reasonable for most measured parameters, it is highly sensitive towards the feed salinity. If C_F varies by $\pm$ 5% ($\pm$ 0.06 mol/L), then the calculated S value changes drastically, especially at high ΔP. Therefore, it is important to ensure that the initial feed salinity is known and accurately measured throughout the membrane characterization process. Interestingly, S is insensitive to erroneous estimations of k_F and k_D. Similarly, Wong et al. [55] experimentally showed that changes in S due to variations in Q_F and Q_D are insignificant. This can be explained by the fact that ECP is negligible in comparison to ICP.

Besides these six parameters, the temperature of the feed and draw solution is another parameter that indirectly affects the membrane's intrinsic properties. As reasoned by Wong et al. [55], variations in the calculated A, B and S values due to changes in solution temperature may be caused by thermally-induced changes of the membrane structure, such as weakening of intermolecular bonds within the membrane material.

References

[1] C. D. Peters, N. P. Hankins, The synergy between osmotically assisted reverse osmosis (OARO) and the use of thermo-responsive draw solutions for energy efficient, zero-liquid discharge desalination, Desalination 493 (2020) 114630. doi:10.1016/j.desal.2020.114630.

[2] A. T. Bouma, J. H. Lienhard, Split-feed counterflow reverse osmosis for brine concentration, Desalination 445 (2018) 280–291. doi:10.1016/J.DESAL.2018.07.011.

[3] T. V. Bartholomew, L. Mey, J. T. Arena, N. S. Siefert, M. S. Mauter, Osmotically assisted reverse osmosis for high salinity brine treatment, Desalination 421 (2017) 3–11. doi:https://doi.org/10.1016/j.desal.2017.04.012.

[4] H. T. Madsen, S. S. Nissen, J. Muff, E. G. Søgaard, Pressure retarded osmosis from hypersaline solutions: Investigating commercial FO membranes at high pressures, Desalination 420 (2017) 183–190. doi:https://doi.org/10.1016/j.desal.2017.06.028.

[5] A. P. Straub, C. O. Osuji, T. Y. Cath, M. Elimelech, Selectivity and Mass Transfer Limitations in Pressure-Retarded Osmosis at High Concentrations and Increased Operating Pressures, Environmental Science and Technology 49 (2015) 12551–12559. URL: https://pubs.acs.org/doi/abs/10.1021/acs.est.5b01317. doi:10.1021/acs.est.5b01317.

[6] Y. Li, R. Wang, S. Qi, C. Tang, Structural stability and mass transfer properties of pressure retarded osmosis (PRO) membrane under high operating pressures, Journal of Membrane Science 488 (2015) 143–153. doi:10.1016/j.memsci.2015.04.030.

[7] Q. She, X. Jin, C. Y. Tang, Osmotic power production from salinity gradient resource by pressure retarded osmosis: Effects of operating conditions and reverse solute diffusion, Journal of Membrane Science 401-402 (2012) 262–273. doi:10.1016/j.memsci.2012.02.014.

[8] D. M. Davenport, C. L. Ritt, R. Verbeke, M. Dickmann, W. Egger, I. F. Vankelecom, M. Elimelech, Thin film composite membrane compaction

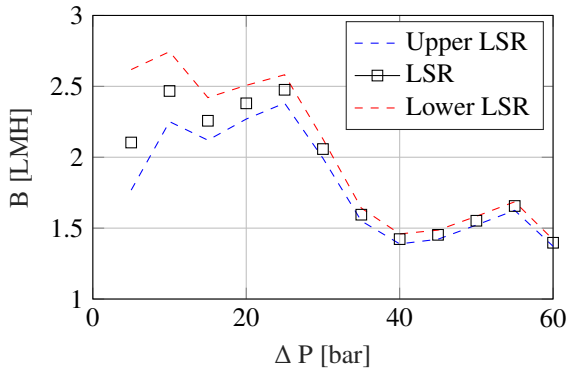

(a) B sensitivity: $\Delta P \pm 1$ bar

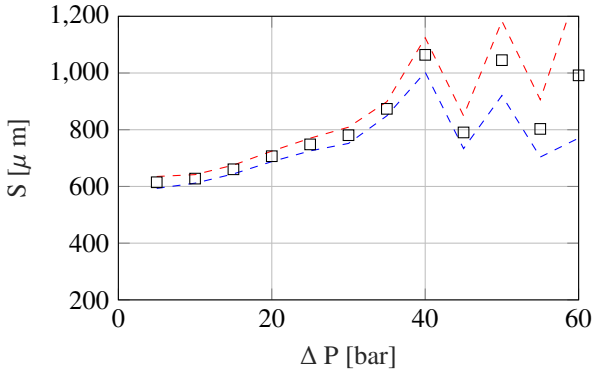

(b) S sensitivity: $\Delta P \pm 1$ bar

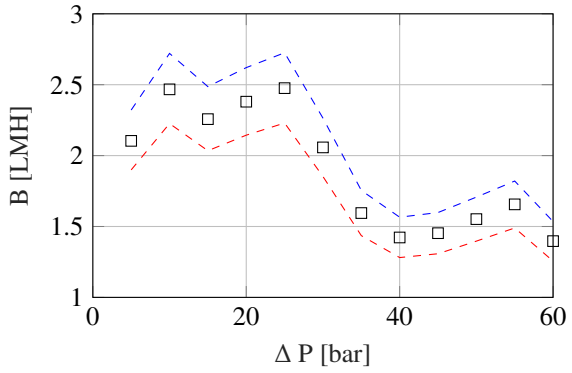

(c) B sensitivity: $\Delta m \pm 10\%$

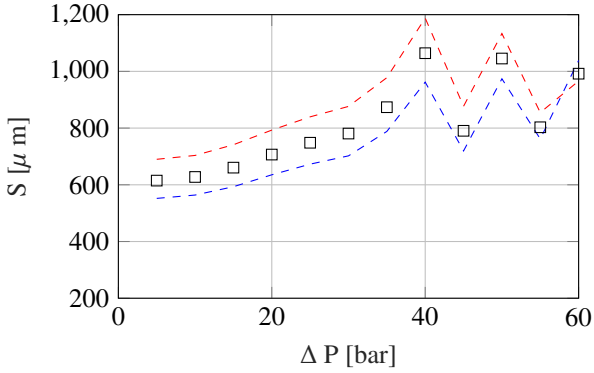

(d) S sensitivity: $\Delta m \pm 10\%$

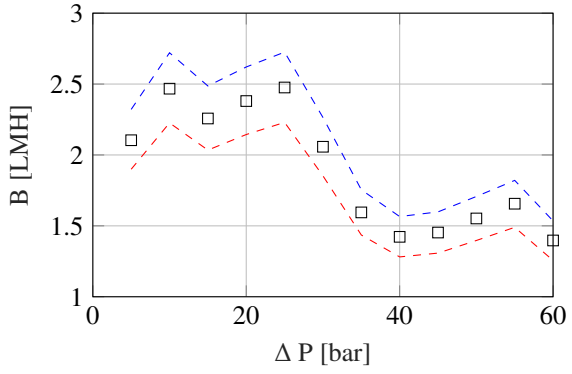

(e) B sensitivity: $C_D \pm 10\%$

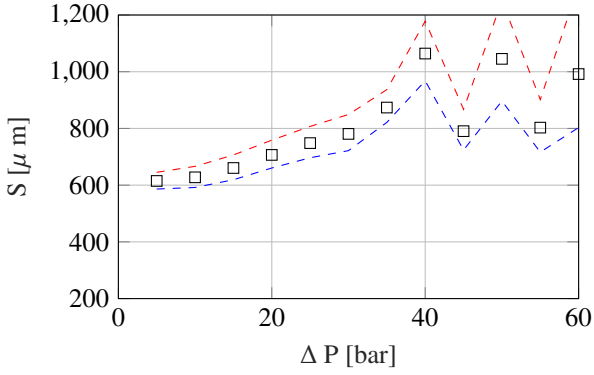

(f) S sensitivity: $C_D \pm 10\%$

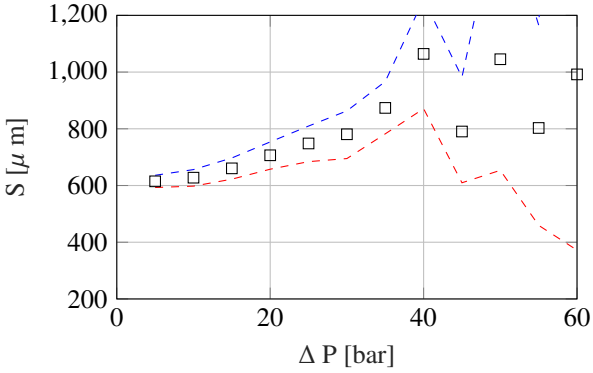

(g) S sensitivity: $C_F \pm 5\%$

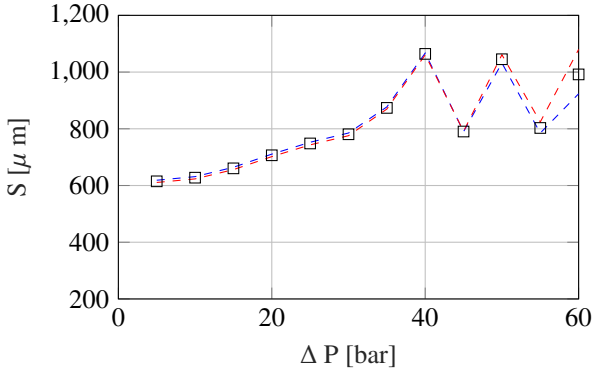

(h) S sensitivity: Q_F and $Q_D \pm 10\%$

Figure B.12: Sensitivity analysis: The effect of measurement inaccuracies on the determined B and S values of the Aquaporin membrane.

in high-pressure reverse osmosis, Journal of Membrane Science 610 (2020) 118268. doi:10.1016/j.memsci.2020.118268.

[9] D. M. Davenport, A. Deshmukh, J. R. Werber, M. Elimelech, High-Pressure Reverse Osmosis for Energy-Efficient Hypersaline Brine Desalination: Current Status, Design Considerations, and Research Needs, Environmental Science & Technology Letters (2018). doi:10.1021/acs.estlett.8b00274.

[10] S. Kook, C. Lee, T. T. Nguyen, J. Lee, H. K. Shon, I. S. Kim, Serially connected forward osmosis membrane elements of pressure-assisted forward osmosis-reverse osmosis hybrid system: Process performance and economic analysis, Desalination 448 (2018) 1–12. doi:10.1016/j.desal.2018.09.019.

[11] S. Jamil, S. Jeong, S. Vigneswaran, Application of pressure assisted forward osmosis for water purification and reuse of reverse osmosis concentrate from a water reclamation plant, Separation and Purification Technology 171 (2016) 182–190. doi:10.1016/j.seppur.2016.07.036.

[12] Y. Oh, S. Lee, M. Elimelech, S. Lee, S. Hong, Effect of hydraulic pressure and membrane orientation on water flux and reverse solute flux in pressure assisted osmosis, Journal of Membrane Science 465 (2014) 159–166. doi:https://doi.org/10.1016/j.memsci.2014.04.008.

[13] G. Blandin, A. R. Verliefde, C. Y. Tang, A. E. Childress, P. Le-Clech, Validation of assisted forward osmosis (AFO) process: Impact of hydraulic pressure, Journal of Membrane Science 447 (2013) 1–11. doi:10.1016/j.memsci.2013.06.002.

[14] M. Aghajani, M. Wang, L. M. Cox, J. P. Killgore, A. R. Greenberg, Y. Ding, Influence of support-layer deformation on the intrinsic resistance of thin film composite membranes, Journal of Membrane Science 567 (2018) 49–57. doi:10.1016/j.memsci.2018.09.031.

[15] E. de Roever, M. Fazel, A. Hallsby, Permeate Spacer Imprints on SWRO Membranes: Evidence for Intrusion and Compaction, IDA Wolrd Congress (2009).

[16] J. A. Idarraga-Mora, A. D. O'Neal, M. E. Pfeiler, D. A. Ladner, S. M. Husson, Effect of mechanical strain on the transport properties of thin-film composite membranes used in osmotic processes, Journal of Membrane Science 615 (2020) 118488. doi:10.1016/j.memsci.2020.118488.

[17] Q. She, J. Wei, N. Ma, V. Sim, A. G. Fane, R. Wang, C. Y. Tang, Fabrication and characterization of fabric-reinforced pressure retarded osmosis membranes for osmotic power harvesting, Journal of Membrane Science 504 (2016) 75–88. doi:10.1016/j.memsci.2016.01.004.

[18] Q. She, D. Hou, J. Liu, K. H. Tan, C. Y. Tang, Effect of feed spacer induced membrane deformation on the performance of pressure retarded osmosis (PRO): Implications for PRO process operation, Journal of Membrane Science 445 (2013) 170–182. doi:10.1016/j.memsci.2013.05.061.

[19] D. G. Callister Jr, William D and Rethwisch, Fundamentals of materials science and engineering: an integrated approach, John Wiley \& Sons, 2020.

[20] D. W. Ward, Ian M and Hadley, An introduction to the mechanical properties of solid polymers, 1993.

[21] T. Y. Cath, M. Elimelech, J. R. McCutcheon, R. L. McGinnis, A. Achilli, D. Anastasio, A. R. Brady, A. E. Childress, I. V. Farr, N. T. Hancock, J. Lampi, L. D. Nghiem, M. Xie, N. Y. Yip, Standard Methodology for Evaluating Membrane Performance in Osmotically Driven Membrane Processes, Desalination 312 (2013) 31–38. doi:10.1016/j.desal.2012.07.005.

[22] C. Y. Tang, Q. She, W. C. Lay, R. Wang, A. G. Fane, Coupled effects of internal concentration polarization and fouling on flux behavior of forward osmosis membranes during humic acid filtration, Journal of Membrane Science 354 (2010) 123–133. doi:10.1016/j.memsci.2010.02.059.

[23] A. Tiraferri, N. Y. Yip, A. P. Straub, S. Romero-Vargas Castrillon, M. Elimelech, A method for the simultaneous determination of transport and structural parameters of forward osmosis membranes, Journal of Membrane Science 444 (2013) 523–538. URL: https://linkinghub.elsevier.com/retrieve/pii/S0376738813004109. doi:10.1016/j.memsci.2013.05.023.

[24] J. Kim, B. Kim, D. Inhyuk Kim, S. Hong, Evaluation of apparent membrane performance parameters in pressure retarded osmosis processes under varying draw pressures and with draw solutions containing organics, Journal of Membrane Science 493 (2015) 636–644. doi:10.1016/j.memsci.2015.07.035.

[25] A. P. Straub, N. Y. Yip, M. Elimelech, Raising the Bar: Increased Hydraulic Pressure Allows Unprecedented High Power Densities in Pressure-Retarded Osmosis, Environmental Science & Technology Letters 1 (2014) 55–59. doi:10.1021/ez400117d.

[26] Y. C. Kim, M. Elimelech, Adverse Impact of Feed Channel Spacers on the Performance of Pressure Retarded Osmosis, Environ. Sci. Technol. 46 (2012) 4673–4681. doi:10.1021/es3002597.

[27] Q. She, L. Zhang, R. Wang, W. B. Krantz, A. G. Fane, Pressure-retarded osmosis with wastewater concentrate feed: Fouling process considerations, Journal of Membrane Science 542 (2017) 233–244. doi:10.1016/j.memsci.2017.08.022.

[28] D. I. Kim, J. Kim, S. Hong, Changing membrane orientation in pressure retarded osmosis for sustainable power generation with low fouling, Desalination 389 (2016) 197–206. doi:10.1016/j.desal.2016.01.008.

[29] M. Zhang, D. Hou, Q. She, C. Y. Tang, Gypsum scaling in pressure retarded osmosis: experiments, mechanisms and implications., Water research 48 (2014) 387–95. URL: http://www.ncbi.nlm.nih.gov/pubmed/24156948. doi:10.1016/j.watres.2013.09.051.

[30] Q. She, Y. K. W. Wong, S. Zhao, C. Y. Tang, Organic fouling in pressure retarded osmosis: Experiments, mechanisms and implications, Journal of Membrane Science 428 (2013) 181–189. doi:10.1016/j.memsci.2012.10.045.

[31] Q. She, R. Wang, A. G. Fane, C. Y. Tang, Membrane fouling in osmotically driven membrane processes: A review, 2016. doi:10.1016/j.memsci.2015.10.040.

[32] G. Blandin, D. T. Myat, A. R. D. Verliefde, P. Le-Clech, Pressure assisted osmosis using nanofiltration membranes (PAO-NF): Towards higher efficiency osmotic processes, Journal of Membrane Science 533 (2017) 250–260. doi:https://doi.org/10.1016/j.memsci.2017.03.048.

[33] D. Xiao, W. Li, S. Chou, R. Wang, C. Y. Tang, A modeling investigation on optimizing the design of forward osmosis hollow fiber modules, Journal of Membrane Science 392-393 (2012) 76–87. doi:https://doi.org/10.1016/j.memsci.2011.12.006.

[34] J. Duan, E. Litwiller, I. Pinnau, Solution-diffusion with defects model for pressure-assisted forward osmosis, Journal of Membrane Science 470 (2014) 323–333. doi:https://doi.org/10.1016/j.memsci.2014.07.018.

[35] J. Wang, D. S. Dlamini, A. K. Mishra, M. T. M. Pendergast, M. C. Y. Wong, B. B. Mamba, V. Freger, A. R. D. Verliefde, E. M. V. Hoek, A critical review of transport through osmotic membranes, Journal of Membrane Science 454 (2014) 516–537. doi:https://doi.org/10.1016/j.memsci.2013.12.034.

[36] G. Schock, A. Miquel, Mass transfer and pressure loss in spiral wound modules, Desalination 64 (1987) 339–352. doi:10.1016/0011-9164(87)90107-X.

[37] B. Dutta, Principles of mass transfer and seperation processes, 2007.

[38] T. V. Bartholomew, N. S. Siefert, M. S. Mauter, Cost Optimization of Osmotically Assisted Reverse Osmosis, Environmental Science and Technology (2018). doi:10.1021/acs.est.8b02771.

[39] B. Kim, G. Gwak, S. Hong, Review on methodology for determining forward osmosis (FO) membrane characteristics: Water permeability (A), solute permeability (B), and structural parameter (S), 2017. doi:10.1016/j.desal.2017.08.006.

[40] DOW Water Solutions, Filmtec Membranes: Product Information Catalog, 2020.

[41] Y. A. Hussain, M. H. Al-Saleh, A viscoelastic-based model for TFC membranes flux reduction during compaction, Desalination 344 (2014) 362–370. doi:10.1016/j.desal.2014.04.010.

[42] V. E. Reinsch, A. R. Greenberg, S. S. Kelley, R. Peterson, L. J. Bond, A new technique for the simultaneous, real-time measurement of membrane compaction and performance during exposure to high-pressure gas, Journal of Membrane Science 171 (2000) 217–228. doi:10.1016/S0376-7388(00)00307-0.

[43] M. T. M. Pendergast, J. M. Nygaard, A. K. Ghosh, E. M. Hoek, Using nanocomposite materials technology to understand and control reverse osmosis membrane compaction, Desalination 261 (2010) 255–263. doi:10.1016/j.desal.2010.06.008.

[44] D. Y. F. Ng, Y. Chen, Z. Dong, R. Wang, Membrane compaction in forward osmosis process, Desalination 468 (2019) 114067. doi:10.1016/j.desal.2019.07.007.

[45] N. Y. Yip, M. Elimelech, Performance Limiting Effects in Power Generation from Salinity Gradients by Pressure Retarded Osmosis, Environmental Science & Technology 45 (2011) 10273–10282.

doi:10.1021/es203197e.

[46] J. R. Werber, A. Deshmukh, M. Elimelech, The Critical Need for Increased Selectivity, Not Increased Water Permeability, for Desalination Membranes, Environmental Science & Technology Letters 3 (2016) 112–120. doi:10.1021/acs.estlett.6b00050.

[47] S. S. Manickam, J. R. McCutcheon, Model thin film composite membranes for forward osmosis: Demonstrating the inaccuracy of existing structural parameter models, Journal of Membrane Science 483 (2015) 70–74. doi:10.1016/j.memsci.2015.01.017.

[48] L. Xia, M. F. Andersen, C. Hélix-Nielsen, J. R. McCutcheon, Novel Commercial Aquaporin Flat-Sheet Membrane for Forward Osmosis, Industrial and Engineering Chemistry Research 56 (2017) 11919–11925. URL: https://pubs.acs.org/sharingguidelines. doi:10.1021/acs.iecr.7b02368.

[49] M. Nikbakht Fini, H. T. Madsen, J. L. Sørensen, J. Muff, Moving from lab to pilot scale in forward osmosis for pesticides rejection using aquaporin membranes, Separation and Purification Technology 240 (2020) 116616. doi:10.1016/j.seppur.2020.116616.

[50] M. Xie, W. Luo, H. Guo, L. D. Nghiem, C. Y. Tang, S. R. Gray, Trace organic contaminant rejection by aquaporin forward osmosis membrane: Transport mechanisms and membrane stability, Water Research 132 (2018) 90–98. doi:10.1016/j.watres.2017.12.072.

[51] S. Sahebi, M. Sheikhi, B. Ramavandi, A new biomimetic aquaporin thin film composite membrane for forward osmosis: Characterization and performance assessment, Desalination and Water Treatment 148 (2019) 42–50. doi:10.5004/dwt.2019.23748.

[52] Y. Chun, L. Qing, G. Sun, M. R. Bilad, A. G. Fane, T. H. Chong, Prototype aquaporin-based forward osmosis membrane: Filtration properties and fouling resistance, Desalination 445 (2018) 75–84. doi:10.1016/j.desal.2018.07.030.

[53] J. Wei, C. Qiu, C. Y. Tang, R. Wang, A. G. Fane, Synthesis and characterization of flat-sheet thin film composite forward osmosis membranes, Journal of Membrane Science 372 (2011) 292–302. doi:10.1016/j.memsci.2011.02.013.

[54] J. Lee, A. Hill, S. Kentish, Formation of a thick aromatic polyamide membrane by interfacial polymerisation, Separation and Purification Technology 104 (2013) 276–283. doi:10.1016/j.seppur.2012.11.015.

[55] M. C. Wong, K. Martinez, G. Z. Ramon, E. M. Hoek, Impacts of operating conditions and solution chemistry on osmotic membrane structure and performance, Desalination 287 (2012) 340–349. doi:10.1016/j.desal.2011.10.013.

[56] J. R. McCutcheon, R. L. McGinnis, M. Elimelech, Desalination by ammonia-carbon dioxide forward osmosis: Influence of draw and feed solution concentrations on process performance, Journal of Membrane Science 278 (2006) 114–123. doi:10.1016/j.memsci.2005.10.048.

[57] G. D. Mehta, S. Loeb, Performance of permasep B-9 and B-10 membranes in various osmotic regions and at high osmotic pressures, Journal of Membrane Science 4 (1978) 335–349. doi:10.1016/S0376-7388(00)83312-8.

[58] M. F. McCurley, W. R. Seitz, Fiber-optic sensor for salt concentration based on polymer swelling coupled to optical displacement, Analytica Chimica Acta 249 (1991) 373–380. doi:10.1016/S0003-2670(00)83009-3.

[59] N. N. Bui, J. T. Arena, J. R. McCutcheon, Proper accounting of mass transfer resistances in forward osmosis: Improving the accuracy of model predictions of structural parameter, Journal of Membrane Science 492 (2015) 289–302. doi:10.1016/j.memsci.2015.02.001.

[60] Y. A. Hussain, M. H. Al-Saleh, S. S. Ar-Ratrout, The effect of active layer non-uniformity on the flux and compaction of TFC membranes, Desalination 328 (2013) 17–23. doi:10.1016/j.desal.2013.08.008.

[61] M. Hirose, H. Ito, Y. Kamiyama, Effect of skin layer surface structures on the flux behaviour of RO membranes, Journal of Membrane Science 121 (1996) 209–215. doi:10.1016/S0376-7388(96)00181-0.

[62] S. H. Kim, S. Y. Kwak, T. Suzuki, Positron annihilation spectroscopic evidence to demonstrate the flux-enhancement mechanism in morphology-controlled thin-film-composite (TFC) membrane, Environmental Science and Technology 39 (2005) 1764–1770. URL: https://pubs.acs.org/doi/abs/10.1021/es049453k. doi:10.1021/es049453k.

[63] V. Freger, Swelling and morphology of the skin layer of polyamide composite membranes: An atomic force microscopy study, Environmental Science and Technology 38 (2004) 3168–3175. URL: https://pubs.acs.org/doi/abs/10.1021/es034815u. doi:10.1021/es034815u.

[64] C. Y. Tang, Y. N. Kwon, J. O. Leckie, Effect of membrane chemistry and coating layer on physiochemical properties of thin film composite polyamide RO and NF membranes. I. FTIR and XPS characterization of polyamide and coating layer chemistry, Desalination 242 (2009) 149–167. doi:10.1016/j.desal.2008.04.003.

[65] C. Y. Tang, Y. N. Kwon, J. O. Leckie, Effect of membrane chemistry and coating layer on physiochemical properties of thin film composite polyamide RO and NF membranes. II. Membrane physiochemical properties and their dependence on polyamide and coating layers, Desalination 242 (2009) 168–182. doi:10.1016/j.desal.2008.04.004.

[66] N. Y. Yip, A. Tiraferri, W. A. Phillip, J. D. Schiffman, M. Elimelech, High performance thin-film composite forward osmosis membrane, Environmental Science and Technology 44 (2010) 3812–3818. URL: https://pubs.acs.org/sharingguidelines. doi:10.1021/es1002555.

[67] R. A. Peterson, A. R. Greenberg, L. J. Bond, W. B. Krantz, Use of ultrasonic TDR for real-time noninvasive measurement of compressive strain during membrane compaction, Desalination 116 (1998) 115–122. doi:10.1016/S0011-9164(98)00188-X.

[68] L. Brinkert, N. Abidine, P. Aptel, On the relation between compaction and mechanical properties for ultrafiltration hollow fibers, Journal of Membrane Science 77 (1993) 123–131. doi:10.1016/0376-7388(93)85240-W.

[69] X. Zhang, D. G. Cahill, O. Coronell, B. J. Mariñas, Absorption of water in the active layer of reverse osmosis membranes, Journal of Membrane Science 331 (2009) 143–151. doi:10.1016/j.memsci.2009.01.027.

[70] X. Chen, C. Boo, N. Y. Yip, Transport and structural properties of osmotic membranes in high-salinity desalination using cascading osmotically mediated reverse osmosis, Desalination 479 (2020) 114335. doi:10.1016/j.desal.2020.114335.

[71] Y. C. Kim, J. H. Lee, S. J. Park, Novel crossflow membrane cell with asymmetric channels: Design and pressure-retarded osmosis performance test, Journal of Membrane Science 476 (2015) 76–86. doi:10.1016/j.memsci.2014.11.018.

Abbreviations

AL-DS	Active layer on draw side
AL-FS	Active layer on feed side
AQP	Aquaporin
CCP	Concentrative concentration polarisation
CTA	Cellulose triacetate
DCP	Dilutive concentration polarisation
DICP	Dilutive ICP
ECP	External concentration polarisation
FO	Forward osmosis
GLSR	Global least-squares regression
HPRO	High-pressure reverse osmosis
ICP	Internal concentration polarisation
ITS	Integrated two-stage
LSR	Least-squares regression
MED	Median
OARO	Osmotically assisted reverse osmosis
ORF	Osmotic resistance filtration
PAO	Pressure assisted osmosis
PLA	Polylactic acid
PRO	Pressure retarded osmosis
RO	Reverse osmosis

Nomenclature

A	Water permeability coefficient, $L \cdot m^{-2} \cdot s^{-1} \cdot bar^{-1}$
B	Salt permeability coefficient, $L \cdot m^{-2} \cdot h^{-1}$
C_D	Feed concentration , mol/L
C_F	Feed concentration , mol/L
D	Diffusivity coefficient, m^2/s
f_{CCP}	CCP factor
f_{DCP}	DCP factor
F_{App}	Apparent driving force, bar
F_{CCP}	Loss of driving force due to CCP, bar
F_{DCP}	Loss of driving force due to DCP, bar
i	Number of dissociating ions
J_S	Salt flux, $g \cdot m^{-2} \cdot h^{-1}$
J_W	Water flux, $L \cdot m^{-2} \cdot h^{-1}$
k_D	Mass transfer coefficient in draw stream, $L \cdot m^{-2} \cdot h^{-1}$
k_F	Mass transfer coefficient in feed stream, $L \cdot m^{-2} \cdot h^{-1}$
k_M	Mass transfer coefficient in the membrane, $L \cdot m^{-2} \cdot h^{-1}$
Δm	Change in mass measured by scale, kg
Q_D	Draw flowrate, m^3/h
Q_F	Feed flowrate, m^3/h
R_G	Universal gas constant, $J/(mol\,K)$
S	Structural parameter, m
T	Temperature, K
β	Van't Hoff factor
ΔP	Transmembrane pressure difference, bar
$\Delta\pi$	Osmotic pressure difference, bar
$\Delta\pi_{Eff}$	Effective osmotic pressure difference, bar
ϕ	Osmotic coefficient
π_D	Osmotic pressure of draw solution, bar
π_F	Osmotic pressure of feed solution, bar